

THE MAGELLANIC ZOO: MID-INFRARED *SPITZER* SPECTROSCOPY OF EVOLVED STARS AND CIRCUMSTELLAR DUST IN THE MAGELLANIC CLOUDS

G. C. SLOAN¹, K. E. KRAEMER², P. R. WOOD³, A. A. ZIJLSTRA⁴, J. BERNARD-SALAS¹, D. DEVOST^{1,5}, J. R. HOUCK¹

Draft version July 18, 2008

ABSTRACT

We observed a sample of evolved stars in the Large and Small Magellanic Clouds (LMC and SMC) with the Infrared Spectrograph on the *Spitzer Space Telescope*. Comparing samples from the SMC, LMC, and the Galaxy reveals that the dust-production rate depends on metallicity for oxygen-rich stars, but carbon stars with similar pulsation properties produce similar quantities of dust, regardless of their initial metallicity. Other properties of the oxygen-rich stars also depend on metallicity. As the metallicity decreases, the fraction of naked (i.e. dust-free) stars increases, and among the naked stars, the strength of the 8 μ m absorption band from SiO decreases. Our sample includes several massive stars in the LMC with long pulsation periods which produce significant amounts of dust, probably because they are young and relatively metal rich. Little alumina dust is seen in circumstellar shells in the SMC and LMC, unlike in Galactic samples. Three oxygen-rich sources also show emission from magnesium-rich crystalline silicates. Many also show an emission feature at 14 μ m. The one S star in our sample shows a newly detected emission feature centered at 13.5 μ m. At lower metallicity, carbon stars with similar amounts of amorphous carbon in their shells have stronger absorption from molecular acetylene (C₂H₂) and weaker emission from SiC and MgS dust, as discovered in previous studies.

Subject headings: circumstellar matter — infrared: stars

1. INTRODUCTION

In the Galaxy, stars on the asymptotic giant branch (AGB) may be responsible for nearly 90% of the dust injected into the interstellar medium (ISM), with supergiants accounting for most of the remainder (Gehrz 1989). How much these relative contributions change in the early Universe is not well understood. This question has grown even more important, now that the Infrared Spectrograph (IRS Houck et al. 2004) on the *Spitzer Space Telescope* (Werner et al. 2004a) has detected dust in galaxies at redshifts of 2.6–2.7 (Teplitz et al. 2007; Lutz et al. 2007), corresponding to look-back times of ~ 11 Gyr in a Universe 13.7 Gyr old. Supernovae have been suggested as a possible source of dust in the early Universe, (e.g. Cernuschi et al. 1967; Dwek & Scalo 1980), but the amount of dust they contribute remains controversial (e.g. Sugerman et al. 2006; Meikle et al. 2007). The most massive stars that can evolve to the AGB will begin producing dust only ~ 100 Myr after the formation of the first stars in a galaxy. This initial population will be metal poor.

Nearby galaxies within the Local Group give us the opportunity to study how the dust produced by individual supergiants and AGB stars depends on metallicity. The

Large and Small Magellanic Clouds (LMC and SMC) lie at distances of 50 and 61 kpc, respectively (e.g. Alves 2004; Keller & Wood 2006). Measurements of the metallicity ([Fe/H]) of the LMC vary between -0.3 and -0.4 , while the range in the SMC is between -0.6 and -0.8 (Keller & Wood 2006, and references therein).

The *Infrared Space Observatory* (*ISO*) obtained the first mid-infrared spectra of evolved stars in the LMC. Trams et al. (1999) published spectra of 23 targets using the PHOT-S spectrometer, which covered the 2–5 and 6–12 μ m wavelength ranges at a resolution $R \sim 90$ ($R = \lambda/\Delta\lambda$), and the CAM-CVF spectrometer, which observed the 7–14 μ m wavelength range at a resolution of ~ 40 . The formation of CO molecules in stellar outflows will exhaust either C or O from the material available to form dust and divides the dust chemistry around these objects into oxygen-rich or carbon-rich. The *ISO* sample includes spectra from both chemistries, and Trams et al. (1999) showed that they could separate these two groups photometrically with color-color diagrams.

The spectrometers on *ISO* allowed observations of only the brightest targets. The improved sensitivity of the IRS on *Spitzer* has made possible more detailed studies of mass-loss and dust injection in both the LMC and SMC. The five major programs have observed a combined total of 176 sources in the LMC and 63 in the SMC, most of them evolved stars. Sloan et al. (2008a) reviewed these programs and the different criteria used to select targets.

Program 3426 (P.I. Kastner) focused on the brightest sources in the LMC, using the classes defined from observations of the *Mid-Course Space Experiment* (*MSX*) by Egan et al. (2001) (Kastner et al. 2006; Buchanan et al. 2006). Program 3591 (P.I. Kemper) targeted objects covering the stages of evolution of oxygen-rich stars from the AGB to planetary nebulae (Leisenring et al. 2008; Markwick-Kemper et al. 2008). Program 3277

¹ Cornell University, Astronomy Department, Ithaca, NY 14853-6801, sloan@isc.astro.cornell.edu, jbs@isc.astro.cornell.edu, jrh13@cornell.edu

² Air Force Research Laboratory, Space Vehicles Directorate, 29 Randolph Road, Hanscom AFB, MA 01731

³ Research School of Astronomy and Astrophysics, Australian National University, Cotter Road, Weston Creek ACT 2611, Australia, wood@mso.anu.edu.au

⁴ Univ. of Manchester, School of Physics & Astronomy, P. O. Box 88, Manchester M60 1QD, albert.zijlstra@manchester.ac.uk

⁵ Canada France Hawaii Telescope, 65-1238 Mamalahoa Hwy, Kamuela, HI, 96743, devost@cfht.hawaii.edu

TABLE 1
THE MC_DUST PROGRAM

Object Class	LMC		SMC	
	Planned	Observed	Planned	Observed
AGB/M	7	7	4	4
AGB/MS	3	3	4	4
AGB/S	3	2	1	1
AGB/C	6	4	4	1
OH/IR star	3	3
C/IR star	3	2
RSG	3	4	...	1
YSO	...	1
unknown	...	1
total	28	27	13	11

(P.I. Egan) selected targets in the SMC based on their infrared colors (Kraemer et al. 2005, 2006; Sloan et al. 2006b). Program 3505 (P.I. Wood) spanned a range of mass-loss rates in the LMC and the SMC. It included a young stellar object (YSO; van Loon et al. 2005b), but nearly all of the rest are carbon stars (Zijlstra et al. 2006; Matsuura et al. 2006; Groenewegen et al. 2007; Lagadec et al. 2007). The other three programs also observed more carbon stars than initially planned, with sources classified photometrically as OH/IR stars turning out to be carbon stars instead.

This paper focuses on Program 200, (P.I. Sloan; hereafter referred to as the MC_DUST program). The next section describes the sample and the ground-based support observations. In §3, we describe the IRS observations, the data reduction, and the classification of the spectra. The MC_DUST sample contains a rich variety of object types, each of which requires a different method of analysis. We examine each of these types in turn in the following sections: §4—stars with no associated dust (naked stars), §5—dusty oxygen-rich stars, §6—carbon stars, §7—red sources with emission from polycyclic aromatic hydrocarbons (PAHs). Several targets show characteristics which place them in multiple categories, and as a consequence, they will be analyzed in more than one of the following sections. In each of these sections, we examine individual sources and unusual spectral features, but we save a more general comparison of the various populations for §8. Finally, we draw conclusions in §9.

2. THE SAMPLE

2.1. Sample Selection

The MC_DUST program was a small (17.2 hour) program conducted as part of the IRS Guaranteed Time Observations (GTO). It sampled sources in the LMC and SMC covering a range of classifications determined in both the optical and the infrared. The targets were divided into seven classes: red supergiants (RSGs), four categories of optically identified AGB sources (M giants, MS stars, S stars, and C stars), and two categories of infrared sources: OH/IR stars and infrared carbon-rich sources (C/IR stars). Table 1 breaks down the observing program by object class, as planned and as actually executed. The plan included 28 sources in the LMC (20 oxygen-rich and eight carbon-rich), and 13 in the SMC (nine oxygen-rich and four carbon-rich). As with other programs in the Magellanic Clouds, the crowded regions resulted in several peak-up failures. In our case, we lost

three objects in the LMC and three in the SMC, but gained three serendipitous observations, two in the LMC and one in the SMC.

The other spectroscopic samples in the Magellanic Clouds were selected primarily from near- and mid-infrared photometry, but most of the sources in the MC_DUST sample were selected based on optical spectral classifications, supplemented with longer wavelength data. While many of the object types in other programs turned out to be different than planned, our sources, for the most part, had the photospheric chemistries we had expected. Another advantage was that we were able to observe several sources below the photometric limits of previous infrared surveys, allowing us to probe fainter sources on the AGB.

Table 2 lists the individual targets in the MC_DUST sample. The targets with Harvard Variable numbers and the carbon star CV 78⁶ were selected from the study by Wood et al. (1983). These targets account for most of the sources in the RSG, AGB/M and AGB/MS classes. The AGB/S and AGB/C stars with WBP numbers were selected from the observations of Wood et al. (1985). Wood et al. (1983) identified MACHO 79.5505.26 as HV 5680, but HV 5680 is actually 16'' to the northeast and a magnitude fainter at K. The target we have named BFM 1 was the first S star identified in the SMC (Blanco et al. 1981) and, as discussed below, is the only true S star in our sample.⁷ We also selected six oxygen-rich infrared sources first studied by Wood et al. (1992). They identified three as OH/IR stars. The other three include a suspected supergiant (IRAS 04530) and two luminous and embedded evolved stars (IRAS 04509 and IRAS 04516). Finally, we selected three sources believed to be infrared carbon stars (C/IR) from a sample studied by van Loon et al. (1999). The types in parentheses in Table 2 have changed, as discussed in §3.3 and 3.4 below.

Peak-up failures affected our sample of carbon stars most significantly, reducing our LMC sample from eight to six carbon stars and our SMC sample from four to one. Fortunately, other programs produced a surplus of carbon stars, which has resulted in a series of papers on carbon stars in the SMC (Sloan et al. 2006b; Lagadec et al. 2007) and the LMC (Zijlstra et al. 2006; Leisenring et al. 2008). Three of the peak-up failures resulted in serendipitous observations. Instead of observing NGC 371 LE 28 in the SMC, we observed Massey SMC 59803, a supergiant with a spectral class of K2–3 I (Levesque et al. 2006). In the LMC, we observed the giant WOH G 339 instead of WBP 51, and instead of WBP 116, we observed a source identified only in the 2MASS catalog (2MASS J05283210-6929084, or J052832 for short). Little is known about this last source; it may even be a foreground object and not in the SMC.

2.2. Ground-based Spectroscopy

To verify the overall chemistry of our targets, we obtained optical spectra using the Double Beam Spectrograph on the 2.3 m telescope of the Australian National University at Siding Spring Observatory (SSO) of all of our targets, except for seven of the nine IRAS sources,

⁶ CV = Cordoba Variable; Wood et al. (1983) cite Dessy (1959).

⁷ Table 2 corrects the erroneous coordinates for BFM 1 given by Blanco et al. (1981).

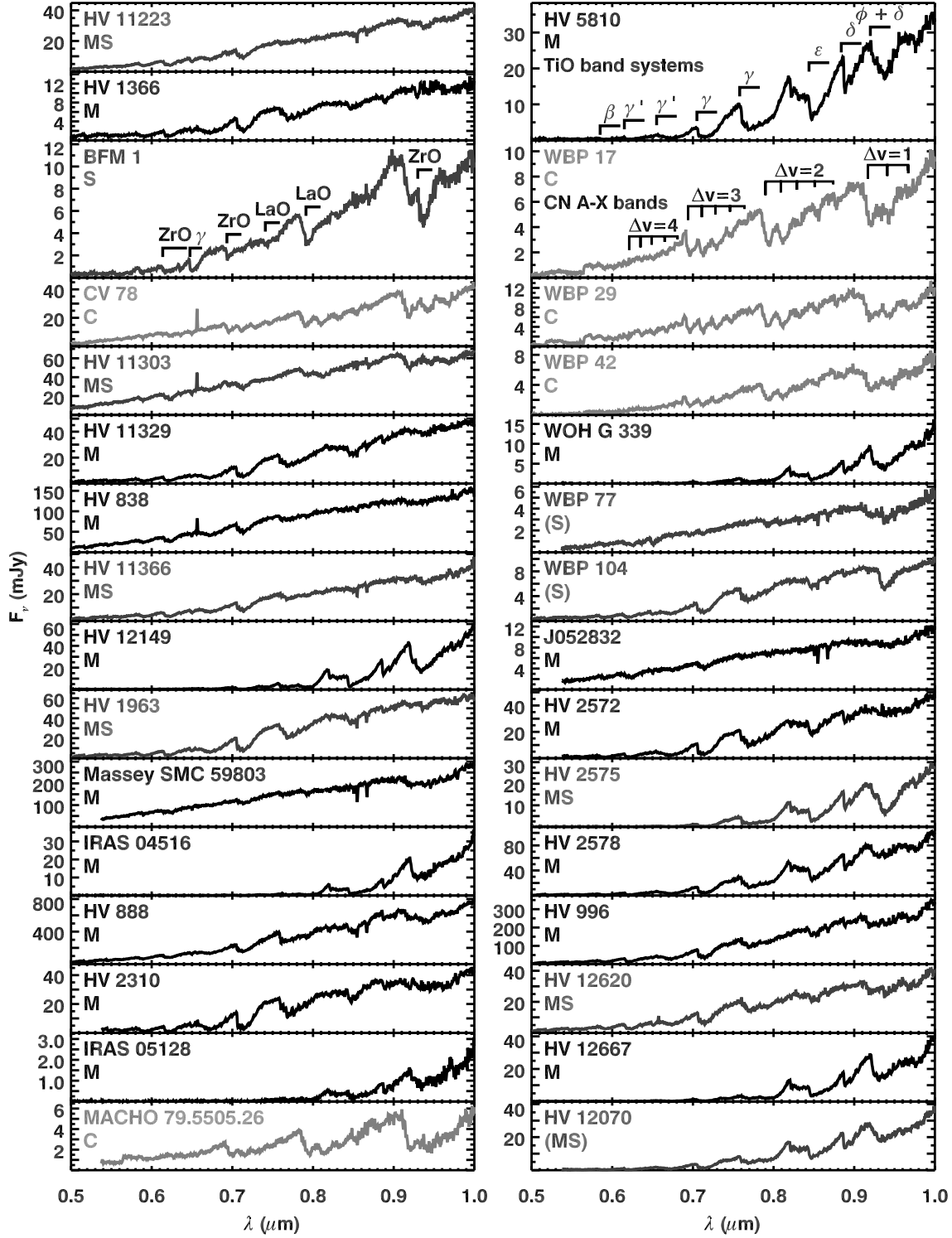


FIG. 1.— Optical spectra of our sample of evolved stars in the Magellanic Clouds. The panels for HV 5810, BFM 1, and WBP 17 are larger than the rest to illustrate typical molecular bands in M giants, S stars, and carbon stars, respectively. Spectral classes in parentheses are inconsistent with the observed spectra. We observed only two of the nine IRAS sources due to the heavy optical obscuration.

TABLE 2
THE MC_DUST SAMPLE

Target	RA J2000.0	Dec.	J	2MASS H	K _s	Source Type	Period (days)	Ref. ^a
HV 11223	00 32 01.61	−73 22 34.7	11.166	10.276	9.971	AGB/MS	407:	1
HV 1366	00 42 49.87	−72 55 11.4	12.232	11.431	11.154	AGB/M	305	5
BFM 1	00 47 19.24	−72 40 04.5	12.661	11.647	11.027	AGB/S	398	5
CV 78	00 49 03.94	−73 05 19.9	11.649	10.613	10.129	AGB/C	423	6
HV 11303	00 52 08.84	−71 36 24.0	10.836	9.983	9.540	AGB/MS	534	1
HV 11329	00 53 39.40	−72 52 39.2	10.911	9.987	9.647	AGB/M	377	5
HV 838	00 55 38.22	−73 11 41.1	10.608	9.860	9.440	AGB/M	622	5
HV 11366	00 56 54.77	−72 14 08.6	11.066	10.154	9.870	AGB/MS	366	1
HV 12149	00 58 50.17	−72 18 35.6	9.963	9.022	8.609	AGB/M	745	5
HV 1963	01 04 26.63	−72 34 40.3	10.638	9.677	9.409	AGB/MS	249	6 ^b
Massey SMC 59803	01 04 38.21	−72 01 27.0	9.093	8.301	8.097	RSG
IRAS 04509−6922	04 50 40.47	−69 17 31.9	9.874	8.670	7.928	(AGB/M)	1290	3
IRAS 04516−6902	04 51 29.00	−68 57 50.1	9.927	8.619	7.914	(AGB/M)	1170	5
IRAS 04530−6916	04 52 45.67	−69 11 49.5	13.942	11.859	9.959	(RSG)	1260:	3
IRAS 04545−7000	04 54 10.06	−69 55 58.3	16.510	12.815	10.402	OH/IR	1270	3
HV 888	05 04 14.14	−67 16 14.4	8.010	7.188	6.781	RSG	850	1
HV 2310	05 06 27.68	−68 12 03.7	10.455	9.635	9.111	AGB/M	600	5
IRAS 05128−6455	05 13 04.57	−64 51 40.3	14.553	12.832	11.281	(C/IR)	708	4
MACHO 79.5505.26	05 14 29.83	−68 54 33.8	12.302	11.363	10.923	AGB/C	97	5 ^b
HV 5810	05 24 07.02	−69 23 36.9	10.813	9.947	9.642	AGB/M	374	5
WBP 17	05 26 19.88	−69 41 37.3	12.342	11.315	10.796	AGB/C	304	5
WBP 29	05 26 40.95	−69 23 11.4	12.270	11.382	10.915	AGB/C	247	5 ^b
WBP 42	05 27 04.73	−69 38 16.3	13.800	12.192	11.009	AGB/C	404	5
WOH G 339	05 27 10.24	−69 36 26.7	10.399	9.544	9.159	AGB/M	538	5
WBP 77	05 28 06.75	−69 32 27.9	12.313	11.482	11.197	AGB/S	212	5
WBP 104	05 28 26.73	−69 14 43.5	12.364	11.422	11.047	AGB/S	245	2
2MASS J052832	05 28 32.10	−69 29 08.5	11.429	10.571	10.326	unknown	110:	5
HV 2572	05 28 36.71	−69 20 04.1	9.795	8.836	8.447	AGB/M	591:	6
HV 2575	05 29 59.98	−67 45 01.4	11.482	10.556	10.066	AGB/MS	390	5
HV 2578	05 29 03.15	−69 48 06.9	9.947	9.104	8.737	AGB/M	653	5 ^b
IRAS 05300−6651	05 30 03.89	−66 49 24.2	16.895	14.800	12.247	C/IR
HV 996	05 32 35.62	−67 55 09.0	8.991	8.156	7.643	RSG	760	1
IRAS 05329−6708	05 32 51.33	−67 06 52.0	17.285	13.638	11.233	OH/IR	1260	3
HV 12620	05 32 59.92	−70 41 23.6	11.206	10.357	10.052	AGB/MS	326	5
IRAS 05348−7024	05 34 15.99	−70 22 52.5	17.659	15.488	12.851	C/IR
IRAS 05402−6956	05 39 44.89	−69 55 18.1	14.344	11.740	9.789	OH/IR	1390	3
HV 12667	05 49 13.36	−70 42 40.7	10.823	10.019	9.445	AGB/M	645	5
HV 12070	05 52 27.86	−69 14 10.0	10.605	9.754	9.204	AGB/MS	599	5

^a References for periods: (1) Wood et al. (1983); (2) Wood et al. (1985); (3) Wood et al. (1992); (4) Whitelock et al. (2003); (5) from MACHO data (Alcock et al. 1996); (6) from OGLE data (Udalski et al. 1997; Szymáński 2005). ^b The period has changed significantly from previously published values; see §2.3.

due to their heavy optical obscuration. These spectra covered the 0.45–1.05 μm wavelength range with a resolution of 10 Å. They were reduced using standard IRAF procedures with HR 718 as a flux standard and the weak-lined giant HD 26169 to remove telluric features. Figure 1 presents the optical spectra. We have expanded the panels for HV 5810, BFM 1, and WBP 17 to use them as prototypes for M giants, S stars, and carbon stars, respectively, and make room for labels for the visible molecular bands.

Cyanogen (CN) bands dominate the spectra of the carbon stars and make them easy to distinguish, with its characteristic corrugations. The bands which appear in this wavelength range arise from the $A^2\Pi - X^2\Sigma^+$ electronic transition (Huber & Herzberg 1979). The band systems are labelled with the change in vibrational state, and in each system the vibrational states involved increase to the red. The spectrum of CV 78 includes H α emission at 0.656 μm .

TiO band systems dominate the spectra of the M giants. The identifications of the band systems presented in Figure 1 are from Huber & Herzberg (1979) and the models of M dwarfs by Valenti et al. (1998). The spectra in the sample show a wide range of band strengths. The spectra which are most obscured by dust show only the reddest bands. Some of the spectra show H α emission.

Figure 1 shows that the spectrum of one of our planned C/IR stars, IRAS 05128, is very similar to IRAS 04516 and clearly oxygen-rich. Trams et al. (1999) classified it as a carbon star based on its *ISO*/PHOT-S spectrum, but subsequently, Matsuura et al. (2005) found strong H₂O absorption and possible weak SiO absorption in its 2.9–4.1 μm spectrum. Our optical spectrum confirms their conclusion that IRAS 05128 is oxygen-rich. van Loon et al. (2008) classify IRAS 05128 as an M9 giant.

Blanco et al. (1981) identified BFM 1 as an S star based on a strong LaO band at 0.79 μm . Our spectrum clearly shows both LaO and ZrO bands, but these are superimposed on a CN spectrum (compare BFM 1 to CV 78 just below it). The strong absorption band at 0.93 μm is due to ZrO (Spinrad & Wing 1969, and references therein) and arises from the $b^3\Pi - a^3\Delta$ electronic transition. It is close to the head of the CN $A-X \Delta v=1$ band system, but displaced $\sim 0.2 \mu\text{m}$ to the red, making it easy to identify. The head of the LaO $A^2\Pi_{3/2} - X^2\Sigma^+$ band system at 0.79 μm (Wyckoff & Clegg 1978) coincides with the head of the CN $A-X \Delta v=2$ band system, but the LaO stands out in two ways. First, the LaO band makes the head of the CN band too deep, and second, the $A^2\Pi_{1/2} - X^2\Sigma^+$ band system appears at 0.74 μm . Similarly, the ZrO $B^1\Pi - X^1\Sigma$ band system strengthens the apparent head of the CN $A-X \Delta v=3$ band system at 0.69 μm , but the ZrO γ band system from 0.61 to 0.66 μm makes the identification unambiguous. The γ system arises from the $A^3\Phi - X^3\Delta$ transition (Phillips & Davis 1979).

BFM 1 is the sole true S star in our sample. WBP 77 shows a hint of LaO absorption at 0.79 μm but is otherwise more consistent with an MS spectrum. Both it and WBP 104 show the 0.65 and 0.93 μm ZrO bands seen in many MS spectra. The spectrum of HV 12070, which is classified as an MS star, looks more like the spectrum

of an M giant. We have noted the uncertainties in the classifications by putting them in parentheses in Figure 1, but we have not changed them for two reasons. First, these sources are variable stars and the spectra may have different characteristics at different phases. Second, we do not distinguish between M and MS stars in our analysis below; we consider them as one group of oxygen-rich sources in our analysis. However, the fact that BFM 1 is our sole strong S star is significant. It is the only source where $C/O \approx 1$, which may explain its unusual dust properties (see §5.6).

2.3. Optical Light Curves

Many of the stars in our sample have light curves in the databases from the MACHO Project (Massive Compact Halo Objects; Alcock et al. 1996) and/or the Optical Gravitational Lensing Experiment (OGLE; Udalski et al. 1997; Szymáński 2005). Table 2 includes the periods we have determined from these data. Most of these stars pulsate regularly, or semi-regularly, with periods covering a wide range, from ~ 100 days to ~ 1400 . The red and blue lightcurves sometimes give slightly different periods. We have found that the blue light curves generally produce more self-consistent periods.

Some of the periods have changed significantly from previously published results, primarily because some of the older periods were based on data which did not sample the light curves adequately. Several periods measured by Wood et al. (1983) have changed. HV 1963 had a period of 330 days, but we measure a period of 249 days with the OGLE data. The MACHO data for MACHO 79.5505.26 give a period of 97 days, compared to 151. This source has a longer cycle of 1200 days, so the shorter period must be an overtone mode. The period of HV 2578 has changed from 470 to 247 days, based on the MACHO data. HV 2572 previously had a period of 201 days. The OGLE data are poorly characterized, but a period of 591 days fits the data better than any other. Wood et al. (1985) measured the period of WBP 29 to be 360 days, but we find that the MACHO data are more consistent with a 247-day period. Several other periods have changed by amounts less than 10%.

2.4. Near-infrared Photometry

We obtained ground-based near-infrared photometry for our sources as close in time to the IRS observations as possible. We used CASPIR (McGregor et al. 1994) on the 2.3-m telescope at SSO to obtain images at J (effective wavelength 1.24 μm), H (1.68 μm), K (2.22 μm), and narrow-band L (3.59 μm). Sloan et al. (2006b) describe the calibration methods. Table 3 presents the photometry. It includes two entries for four sources because we observed them twice with the IRS and twice from the ground. The photometric data for WBP 17 are averaged from measurements made before and after the IRS spectroscopy.

3. IRS SPECTROSCOPY

3.1. IRS Observations

We observed all of the sources in our sample with the low-resolution modules on the IRS. These observations were carried out as part of the IRS GTO allocation, which was spread over the first 2.5 years of the *Spitzer*

TABLE 3
NEAR-INFRARED SSO PHOTOMETRY

Target	J	H	Magnitude K	L	Julian Date
HV 11223	11.197±0.017	10.266±0.023	10.077±0.013	9.673±0.081	2453526
HV 1366	12.258±0.019	11.534±0.012	11.305±0.008	10.451±0.196	2453334
BFM 1	12.377±0.034	11.489±0.018	11.082±0.019	10.103±0.164	2453524
BFM 1	12.088±0.013	11.268±0.014	10.830±0.014	10.186±0.157	2453942
CV 78	11.099±0.036	10.168±0.033	9.880±0.012	9.223±0.058	2453527
HV 11303	10.770±0.022	9.846±0.010	9.626±0.012	9.298±0.067	2453530
HV 11329	11.068±0.013	10.007±0.013	9.800±0.012	9.454±0.074	2453527
HV 11329	10.991±0.012	10.000±0.007	9.781±0.018	9.752±0.113	2453915
HV 838	9.824±0.006	9.008±0.003	8.824±0.004	8.607±0.045	2453227
HV 11366	11.135±0.016	10.115±0.015	9.941±0.012	9.673±0.085	2453530
HV 12149	10.701±0.015	9.758±0.009	9.353±0.014	8.643±0.045	2453530
HV 1963	10.606±0.006	9.630±0.005	9.388±0.003	9.233±0.011	2453227
HV 1963	10.711±0.011	9.735±0.007	9.509±0.017	9.368±0.079	2453915
Massey SMC 59803	9.056±0.015	8.254±0.011	8.141±0.012	7.952±0.018	2453530
IRAS 04509–6922	9.959±0.006	8.724±0.011	8.098±0.015	7.071±0.015	2453517
IRAS 04516–6902	10.229±0.008	8.943±0.010	8.334±0.015	7.280±0.017	2453517
IRAS 04530–6916	13.869±0.020	...	9.768±0.033	7.678±0.025	2453135
IRAS 04545–7000	15.900±0.320	...	10.119±0.006	8.083±0.053	2453135
IRAS 04545–7000	14.472±0.026	11.422±0.007	9.397±0.005	7.221±0.016	2453918
HV 888	7.885±0.008	7.014±0.009	6.788±0.026	6.349±0.017	2453532
HV 2310	10.756±0.004	...	9.533±0.005	8.969±0.080	2453135
IRAS 05128–6455	13.316±0.010	11.451±0.010	10.052±0.014	8.186±0.032	2453531
MACHO 79.5505.26	12.419±0.026	...	10.994±0.009	...	2453135
HV 5810	11.289±0.009	10.307±0.012	10.000±0.016	9.534±0.135	2453530
WBP 17	12.454±0.007	11.322±0.011	10.792±0.015	10.322±0.186	2453516
WBP 29	12.555±0.010	11.411±0.011	10.806±0.020	...	2453516
WBP 42	12.797±0.026	11.283±0.012	10.311±0.015	9.168±0.062	2453517
WBP 77	12.562±0.031	...	11.359±0.004	...	2453135
WBP 104	12.387±0.015	11.398±0.013	11.115±0.015	10.641±0.189	2453532
HV 2572	10.079±0.008	...	8.854±0.006	8.418±0.039	2453135
HV 2575	11.446±0.007	10.433±0.010	10.091±0.015	9.501±0.089	2453530
HV 2575	11.391±0.006	10.438±0.004	10.117±0.004	9.649±0.072	2453919
HV 2578	10.085±0.012	9.146±0.013	8.790±0.015	8.199±0.039	2453527
IRAS 05300–6651	...	14.972±0.107	12.532±0.044	9.437±0.086	2453526
HV 996	8.799±0.007	7.910±0.016	7.468±0.014	6.665±0.014	2453526
IRAS 05329–6708	15.096±0.170	...	9.794±0.008	7.445±0.034	2453135
IRAS 05329–6708	15.618±0.074	12.557±0.015	10.504±0.014	8.159±0.023	2453915
HV 12620	11.197±0.007	10.302±0.011	10.104±0.019	9.472±0.085	2453517
IRAS 05348–7024	13.579±0.200	9.226±0.080	2453135
IRAS 05402–6956	13.632±0.013	11.054±0.011	9.289±0.015	7.170±0.017	2453517
HV 12667	10.793±0.006	9.853±0.020	9.354±0.020	8.527±0.037	2453521
HV 12070	10.421±0.003	...	9.157±0.004	8.596±0.041	2453135

mission. As described below, we also followed up some targets in Cycle 3. We observed four stars with possible low-contrast excesses with longer integration times (PID 30332), and we followed up two sources in the MC_DUST program with Short-High (SH) observations to verify the existence of new dust features at 14 μ m (PID 30345). Table 4 summarizes the low-resolution observations, and Table 5 summarizes the SH observations.

3.2. Standard Reduction

Our data reduction began with the S15 version of the data pipeline released by the *Spitzer* Science Center (SSC). Before extracting spectra from the flatfielded images, we subtracted background images and corrected bad pixels. For the Short-Low (SL) data, we used images with the source in the other aperture as the background (aperture differences). Thus, the Short-Low order 1 (SL1) images served as background data for the SL order 2 (SL2) images, and vice versa. For Long-Low, we obtained nod differences, subtracting images with the source in one nod position from images with the source in the same aperture, but in the other nod position. The next step was to correct bad pixels by interpolating from

their neighbors, using the imclean IDL package⁸. Bad pixels are those flagged in the bit-mask images provided with the data release and those flagged as rogues in the rogue masks provided by the SSC.

We extracted spectra from the corrected images using the profile, ridge, and extract routines available in the SSC's *Spitzer* IRS Custom Extractor (SPICE). The spectra were calibrated with spectral corrections generated from observations of the K0 giant HR 6348 for SL and for LL, HR 6348 along with the late K giants HD 166780 and HD 173511 (see Sloan et al. 2008c, for further details). To eliminate pointing-induced discontinuities between the orders, we normalized the various segments to match at the wavelengths where they overlapped. We normalized segments upwards to the presumably best-centered segment. Finally, we trimmed the segments to eliminate untrustworthy data at the ends.

The SH observations required a different reduction method. We used S14 images, subtracted dedicated sky images, and performed full-slit extractions. We calibrated using observations of ξ Dra (K2 III).

⁸ Available from the SSC as irs-clean.

TABLE 4
LOW-RESOLUTION OBSERVATIONS

Target	AOR key	Time (s) SL LL	IRS Camp.	Observed (UT)	Julian Date	Infrared Sp. Class	M_{bol}^a
HV 11223	6019584	112 480	21	2005 Jun 04	2453526	1.N	-6.13
HV 1366	6017024	240 480	14	2004 Oct 25	2453304	1.N	-4.97
BFM 1	6022912	240 480	21	2005 Jun 02	2453524	2.ST:	-5.03
BFM 1 (follow-up)	17398784	1920 2880	33	2006 Jul 26	2453942	2.NO	-5.23
CV 78	6019072	112 480	21	2005 Jun 05	2453527	2.CE	-6.22
HV 11303	6017536	112 480	21	2005 Jun 08	2453530	1.N:	-6.05
HV 11329	6017280	112 480	21	2005 Jun 05	2453527	1.NO	-6.25
HV 11329 (follow-up)	17399296	1440 2880	32	2006 Jun 28	2453915	1.NO	-6.27
HV 838	6017792	56 480	11	2004 Aug 11	2453228	1.N:	-7.37 ^b
HV 11366	6018304	112 480	21	2005 Jun 08	2453530	1.N:O::	-6.22
HV 12149	6019328	56 480	21	2005 Jun 08	2453530	2.SE8	-6.69 ^c
HV 1963	6018048	112 480	10	2004 Jul 18	2453205	1.N:O:	-6.66
HV 1963 (follow-up)	17399040	960 1920	32	2006 Jun 28	2453915	1.N:O	-6.56
Massey SMC 59803	6019840	240 720	21	2005 Jun 08	2453530	2.SE4u	-8.11
IRAS 04509-6922	6022400	56 120	21	2005 May 26	2453517	2.SE8f	-7.66
IRAS 04516-6902	6020096	56 120	21	2005 May 26	2453517	2.SE6f	-7.43
IRAS 04530-6916	6023936	56 56	6	2004 Apr 18	2453114	5.U/SA	-7.78
IRAS 04545-7000	6020352	56 120	6	2004 Apr 18	2453114	3.SAxf	-6.42
HV 888	6015488	56 120	22	2005 Jul 10	2453562	2.SE8tf	-9.01
HV 2310	6014976	112 480	6	2004 Apr 18	2453114	2.SE5xf	-6.13
IRAS 05128-6455	6024192	56 240	23	2005 Aug 09	2453592	2.SE5f	-5.99
MACHO 79.5505.26	6016768	240 480	6	2004 Apr 16	2453112	1.N	-4.50
HV 5810	6014464	112 480	21	2005 Jun 08	2453530	2.U:	-5.64
WBP 17	6023425	240 720	20	2005 Aug 14	2453597	1.NC	-4.63
WBP 29	6021632	240 720	20	2005 Apr 22	2453483	2.CE:	-4.54
WBP 42	6023680	112 480	21	2005 May 26	2453517	2.CE	-4.97
WOH G 339	6022144	112 480	21	2005 May 26	2453517	2.SE5	-6.52 ^d
WBP 77	6021120	240 480	6	2004 Apr 16	2453112	2.SE1:	-4.26
WBP 104	6021376	240 720	22	2005 Jul 10	2453562	1.NO::	-4.53
2MASS J052832	6020864	240 720	22	2005 Jul 10	2453562	1.NO	-5.45 ^d
HV 2572	6014208	56 480	6	2004 Apr 18	2453114	2.SE7 tf:	-6.78 ^e
HV 2575	6016256	112 480	21	2005 Jun 08	2453530	1.N:	-5.51
HV 2575 (follow-up)	17399552	1920 2880	32	2006 Jul 02	2453919	2.NO	-5.51
HV 2578	6014720	56 480	21	2005 Jun 05	2453527	2.SE7tf	-6.88
IRAS 05300-6651	6024704	56 240	21	2005 Jun 04	2453525	3.CR	-5.17
HV 996	6015744	56 120	21	2005 Jun 04	2453526	2.SE7	-8.30
IRAS 05329-6708	6023168	56 120	6	2004 Apr 18	2453114	3.SAxf	-7.06
HV 12620	6016000	240 720	21	2005 May 26	2453517	1.N:	-5.66
IRAS 05348-7024	6024448	56 480	6	2004 Apr 16	2453112	3.CR	-5.62
IRAS 05402-6956	6020608	56 120	21	2005 May 26	2453517	3.SBxf	-7.20
HV 12667	6015232	56 480	21	2005 May 30	2453521	2.SE6 tf:	-6.26
HV 12070	6016512	56 120	6	2004 Apr 16	2453112	2.SE6	-6.48

^a Based on *Spitzer* spectra and SSO photometry (in Table 3), except where noted. ^b Using 2MASS and S³MC photometry gives $M_{bol} = -6.73$. ^c Using 2MASS and S³MC photometry gives $M_{bol} = -7.38$. ^d Using 2MASS and SAGE photometry to replace absent CASPIR photometry. ^e Using 2MASS and SAGE photometry gives $M_{bol} = -7.16$.

TABLE 5
SHORT-HIGH OBSERVATIONS

Target	AOR key	SH Int. Time (s)	IRS Camp.	Observed (UT)	Julian Date
IRAS 04545-7000	17399808	120	32	2006 Jul 01	2453918.4
IRAS 05329-6708	17400320	60	32	2006 Jun 28	2453914.9

3.3. Bolometric Magnitudes

Table 4 also includes the bolometric magnitudes of our sources at the time of observation, which result from an integration of the IRS spectra and the near-infrared SSO photometry. We have assumed a Wien tail to the blue and a Rayleigh-Jeans tail to the red, and a distance modulus of 18.5 to the LMC and 18.9 to the SMC.

Where possible, we have also computed bolometric magnitudes by replacing the SSO data with the

2MASS photometry in Table 2 and 3.6 and 4.5 μ m *Spitzer* photometry from the SAGE survey of the LMC (Meixner et al. 2006) and the S³MC survey of the SMC (Bolatto et al. 2007).⁹ In those cases where the data give a significantly different result, Table 4 includes a note of explanation.

The observational distinction between red supergiants

⁹ SAGE and S³MC stand, respectively, for Surveying the Agents of Galactic Evolution and the *Spitzer* Survey of the SMC.

and oxygen-rich AGB stars is non-trivial. Sources in the Magellanic Clouds have known distances, making luminosity a logical discriminant (pulsation amplitude is another). Wood et al. (1983) estimate that the classic upper limit for AGB sources lies at about $M_{bol} = -7.1$, but as Wood et al. (1992) discussed, some AGB sources can occasionally stray above that limit. The bolometric luminosities in Table 4 suffer from the additional difficulty of variability. We have observed the stars at only one phase, which blurs the -7.1 -magnitude limit somewhat.

For the classifications in Tables 1 and 2, we assume all RSGs exceed the classic limit and show no large-amplitude pulsation, OH maser emission, or Li absorption at $0.67 \mu\text{m}$. The Li absorption indicates that the source has experienced hot-bottom burning, placing it at the high-mass end of the AGB (Smith et al. 1995).

Four of our targets meet all of these constraints. HV 888 and HV 996 are firmly identified supergiants in the LMC (e.g. Wood et al. 1983), as is Massey SMC 59803 in the SMC (Levesque et al. 2006). The fourth source is IRAS 04530, but this source is probably a young stellar object (YSO), as explained in §7.3.

Two more sources meet some, but not all, of the criteria for a supergiant. IRAS 04509 and IRAS 04516 have bolometric luminosities over the AGB limit by our measurements (with both SSO and 2MASS photometry), but Wood et al. (1992) suggested that they were AGB sources, having measured their bolometric luminosities to be -7.30 and -6.77 , and their amplitudes at K to be 1.5 and 1.3 magnitudes, respectively. They noted that very red AGB sources might exceed the -7.1 -magnitude limit slightly. However, they found no evidence of OH maser activity in IRAS 04509, and Marshall et al. (2004) found none in IRAS 04516. Our bolometric luminosities are well above the classic AGB limit, and while both sources have no detected maser activity, their K-band amplitudes are inconsistent with supergiant status. These two sources are as luminous as AGB sources can be, and we suspect that they are massive AGB sources.

Wood et al. (1992) and Whitelock et al. (2003) detected masers in all three targets identified as OH/IR sources in Table 1. IRAS 05329 and IRAS 05402 have bolometric luminosities in some references over the AGB limit, but the presence of maser emission clarifies their status. IRAS 04545 is under the AGB limit in most references.

Two sources show evidence of hot-bottom burning, HV 2572 (Smith et al. 1995; Whitelock & Feast 2000) and HV 12070 (Whitelock et al. 2003), making them massive AGB stars. Wood et al. (1983) suggested that HV 2572 might be a foreground object, but its radial velocity is more consistent with membership in the LMC (P. Wood, private communication).

3.4. Infrared Spectral Classification

The first step in our analysis is to classify each source into one of five broad categories based on the general properties of its infrared spectrum. Each spectrum is then analyzed in more detail, using a method appropriate to its classification.

We applied the classification method developed at Hanscom Field and introduced by Kraemer et al. (2002). This system places a spectrum into one of five numbered groups based on its overall color: 1 for blue spectra dom-

inated by a stellar continuum, 2 for dusty stars, 3 for spectra dominated by warm dust, and 4 and 5 for spectra dominated by progressively cooler dust.¹⁰ It then describes the dominant features in the spectra with one- or two-letter abbreviations: N for naked stars, SE for silicate emission, SB for self-absorbed silicate emission, SA for silicate absorption, CE for carbon-rich dust emission, CR for optically thick and cooler carbon dust shells, and U for spectra showing the unidentified infrared (UIR) emission features arising from polycyclic aromatic hydrocarbons (PAHs) and related material. We introduce a new classification, 2.ST, in §5.6.

Table 4 gives the infrared spectral classifications, which include the basic classification plus additional subdivisions and notes as described in the following sections. The overall classification determines the method(s) applied to analyze the spectra and in which sections they are discussed. In §4, we discuss the naked stars (1.N and 1.NO) and some of the nearly naked spectra showing other dust features. In §5 we examine oxygen-rich dust spectra (2.SE, 3.SE, 3.SB, and 3.SA), while §6 examines carbon-rich spectra (1.NC, 2.CE and 3.CR). Finally, §7 looks at the spectra with red continua and/or contributions from PAHs.

Distinguishing the nature of the dust (oxygen-rich vs. carbon-rich) is straightforward if there is plenty of dust, but for sources with low-contrast excesses, not only can it be difficult to determine what kind of dust is present, but it can be a challenge just to decide if there is an excess at all. To assist, we have measured the dust emission contrast (DEC), which Sloan & Price (1995) defined to be the ratio of dust emission to stellar emission between 7.67 and $14.03 \mu\text{m}$. They applied this method to the database of Low-Resolution Spectra (LRS) from *IRAS*. Sloan & Price (1998) noted that all sources with $\text{DEC} > 0.08$ had clear dust excesses, while all sources with $\text{DEC} < 0.04$ looked naked. The sources between these two limits were more problematic and could be described as “fig-leaf” sources, since they are neither naked nor fully clothed by a dust shell.

We follow their example, but with some changes. As done previously, we assume the optically thin case, which implies that the contributions to the spectrum from the star and dust are additive. The better coverage to shorter wavelengths of the IRS compared to the LRS allows us to shift the wavelength range for fitting the stellar contribution to $6.8\text{--}7.4 \mu\text{m}$, between an absorption band from water vapor at $\sim 6.6 \mu\text{m}$ and the fundamental SiO band, which begins at $7.4 \mu\text{m}$. As discussed below (§4), the SiO band is much weaker in the Magellanic Clouds than in the Galaxy, so instead of using a model spectrum with an SiO band, we simply fit and subtract a 3600 K Planck function to measure the DEC. This also makes the method general enough to apply to carbon stars.

While Sloan & Price (1998) set the minimum DEC for dusty stars to be 0.08, we find that in the MC_DUST sample, sources with a DEC as high as 0.10 do not have a sufficient excess to identify unambiguously. We classify sources with $\text{DEC} \leq 0.04$ as 1.N, while the fig-leaf sources with $0.04 < \text{DEC} \leq 0.10$ are 1.N:. Sources with higher dust

¹⁰ These last two groups are distinguished using data from 36 to $45 \mu\text{m}$, which are unavailable to the IRS. We simply classify the one red spectrum as group 5.

emission contrasts are classified in group 2, and in all cases but one, can be placed into the appropriate subcategory (2.SE, 2.CE, etc.).

Three sources (BFM 1, HV 5810, and WBP 77) have DECs high enough to qualify as dusty, but we can see through the dust and investigate their photospheres. Consequently, we will examine their photospheric properties in the section below on naked stars (§4) and their dust content in the appropriate section as well.

Two of our sources are identified as C/IR stars in Table 2, IRAS 05300 and IRAS 05348. van Loon et al. (2006) list IRAS 05348 as “unknown type”, but our IRS data clearly show a carbon star. As noted in §2.2, IRAS 05128 has previously been identified as carbon-rich based on its *ISO* spectrum, but both our optical and infrared spectra reveal an oxygen-rich source.

One source, MACHO 79.5505.26, has inconsistent optical and infrared spectra. The optical spectrum is clearly carbon-rich, but the infrared spectrum shows no dust or absorption bands indicating its chemistry, which is unusual for carbon stars. For this reason, we analyze it both in §4 and 6. Similarly, the SMC supergiant Massey SMC 59803 shows both silicate and PAH emission (analyzed separately in §5 and 7).

4. NAKED STARS

Figures 2 and 3 present the spectra of the naked sources in the SMC and LMC, respectively. These include seven of the 11 SMC LMCs and five of the 27 LMC sources.

Many of these spectra are faint, which exposes us to background issues that would have little effect on brighter sources. The Magellanic Clouds are crowded in the infrared, with extended emission and a multitude of stray sources. These have a greater impact on LL, with its 10'' slit and sensitivity to extended emission from cool dust. In some of the spectra, the source is faint enough and blue enough that we failed to detect it in LL. For this reason, our analysis will concentrate on the SL data. Even though some of the LL data are excellent, we did not detect any significant spectral features beyond about 15 μm .

4.1. Method

The Hanscom system includes two subclasses of naked stars, oxygen-rich (1.NO), and carbon-rich (1.NC). The 1.NO spectra can be distinguished by the presence of the SiO fundamental band, with maximum absorption at 8.0 μm . For 1.NC spectra, the primary discriminant is the acetylene (C_2H_2) absorption band at 7.5 μm , and in some cases, a narrower acetylene band at 13.7 μm . Those sources which cannot be identified as 1.NO or 1.NC are classified simply as 1.N. We examine the one 1.NC spectrum, of WBP 17, in §6.

The SiO fundamental has a bandhead at 7.4 μm . While the wavelength of maximum absorption is nearby, at 8.0 μm , the band extends out as far as ~ 11.0 μm in some cases. The band is broad enough, and the spectra are noisy enough, that our usual technique of fitting a line segment to the continuum on either side of the band to integrate the equivalent width is inadequate. First, the continuum is not linear over such a broad wavelength range, and second, our estimated equivalent width has proven too sensitive to the vagueries of the continuum fit. Instead, we have constructed a template transmis-

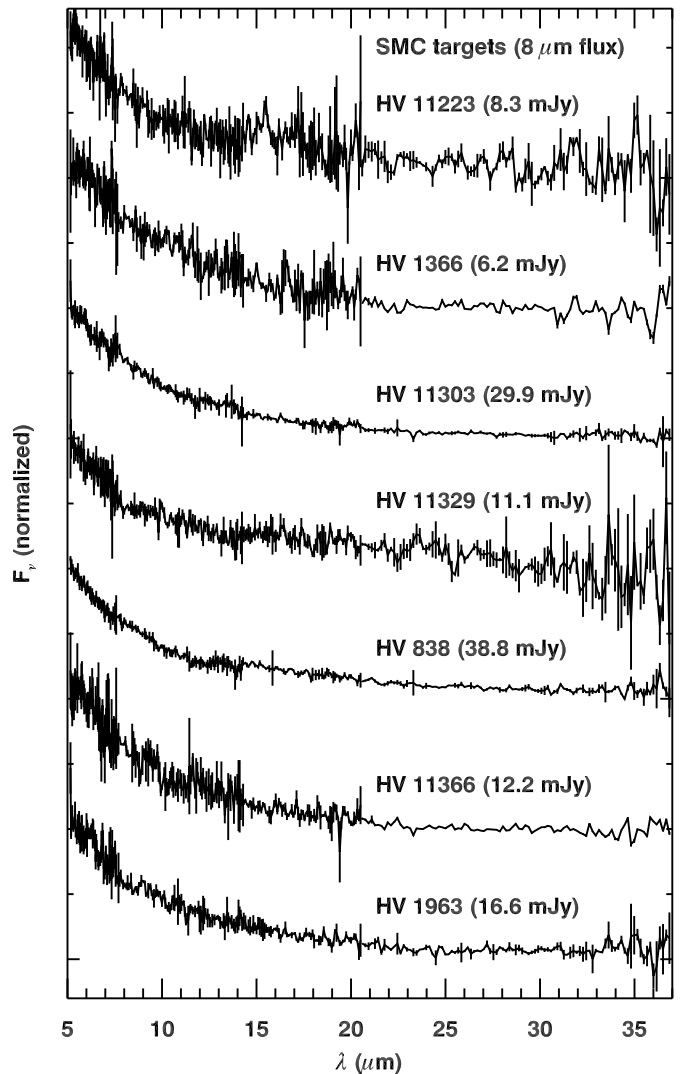


FIG. 2.— IRS spectra of naked oxygen-rich stars in the SMC. The spectra have been normalized and shifted for clarity. The 8 μm flux, determined by applying the bandpass of the IRAC 8 μm filter to the IRS data, is given after each source name in parentheses.

sion spectrum from Cycle 4 IRS GTO observations of 10 naked M giants (PID 40112; Sloan et al. 2008d) and fitted it to the spectrum to estimate the equivalent width.¹¹ We estimate the continuum with a Planck function which reproduces the color measured over the wavelength intervals 6.10–6.45 and 11.5–13.0 μm . We then scale the transmission spectrum until we find the minimum χ^2 difference, and measure the equivalent width of our fitted spectrum from 7.4 to 11.5 μm . We estimate the uncertainty in the fitted temperature by varying the long-wavelength fitting interval, and we estimate the uncertainty in equivalent width by finding the SiO strengths which correspond to the minimum χ^2 multiplied by the factor $(1 + N^{-1/2})$, where N is the number of pixels in the measured wavelength range.

Figures 4 and 5 illustrate the best fits to the naked stars, and Figure 6 shows the three sources with both possible low-contrast dust and photospheric absorption

¹¹ The sample currently includes 13 reduced spectra, but we did not use three with strong water vapor absorption at 6.6 μm when generating the SiO template.

TABLE 6
NAKED AND NEARLY NAKED STARS

Target	Dust Em. Contrast	Fitted T (K)	W_λ SiO (μm)	Infrared Sp. Class
HV 11223	-0.02 ± 0.08	2290 ± 510	< 0.18	1.N
HV 1366	0.02 ± 0.06	2270 ± 560	< 0.20	1.N
BFM 1	0.24 ± 0.04	1460 ± 110	< 0.16	2.ST:
BFM 1 (follow-up)	0.16 ± 0.02	1160 ± 10	0.15 ± 0.05	2.N:O
HV 11303	0.07 ± 0.03	2130 ± 240	< 0.03	1.N:
HV 11329	0.04 ± 0.05	1600 ± 80	0.28 ± 0.13	1.NO
HV 11329 (follow-up)	0.00 ± 0.02	2380 ± 100	0.18 ± 0.03	1.NO
HV 838	0.10 ± 0.03	2320 ± 320	< 0.02	1.N:
HV 11366	0.06 ± 0.09	2230 ± 300	0.18 ± 0.19	1.N:O::
HV 1963	0.07 ± 0.05	2160 ± 120	0.21 ± 0.13	1.N:O:
HV 1963 (follow-up)	0.05 ± 0.01	1990 ± 50	0.13 ± 0.03	1.N:O
MACHO 79.5505.26	-0.06 ± 0.04	4120 ± 2170	< 0.11	1.N
HV 5810	0.19 ± 0.08	1210 ± 110	0.38 ± 0.17	2.U
WBP 77	0.19 ± 0.07	1130 ± 120	0.33 ± 0.18	2.SE1:
WBP 104	-0.11 ± 0.06	4080 ± 890	0.20 ± 0.19	1.NO::
2MASS J052832	-0.21 ± 0.05	$10000 \pm \dots$	0.34 ± 0.15	1.NO
HV 2575	0.07 ± 0.07	2170 ± 870	0.09 ± 0.17	1.N:
HV 2575 (follow-up)	0.07 ± 0.02	2260 ± 180	0.24 ± 0.08	1.N:O
HV 12620	0.06 ± 0.03	1900 ± 10	< 0.04	1.N:

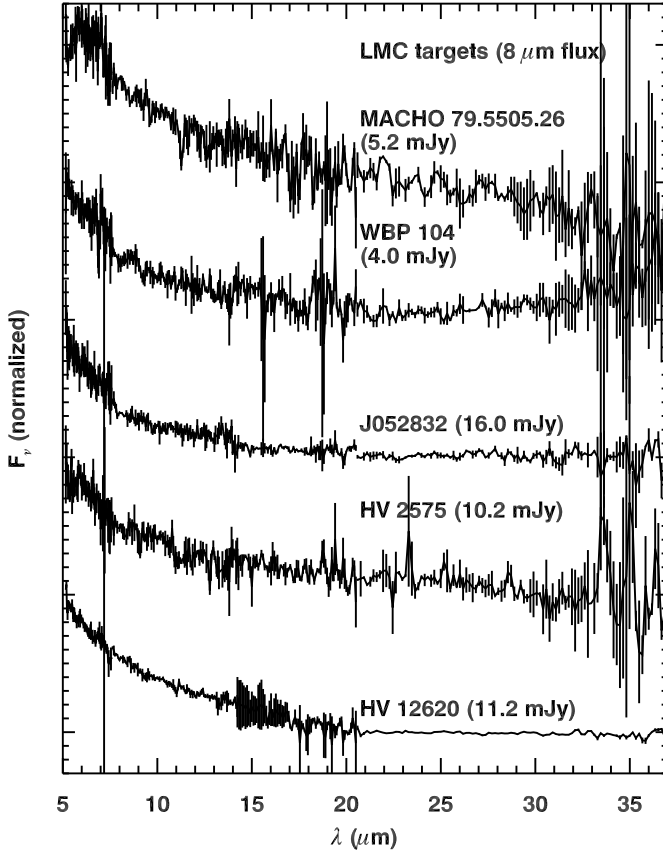


FIG. 3.— IRS spectra of naked oxygen-rich stars in the LMC. As in Fig. 2, the spectra have been normalized and shifted.

bands. The results of these fits appear in Table 6.

4.2. Results

For each naked spectrum, Table 6 lists the dust emission contrast, the temperature of the fitted Planck function, and the equivalent width of the best-fitting SiO band. One should not overinterpret the temperatures. Spectra from sources which were not properly centered in

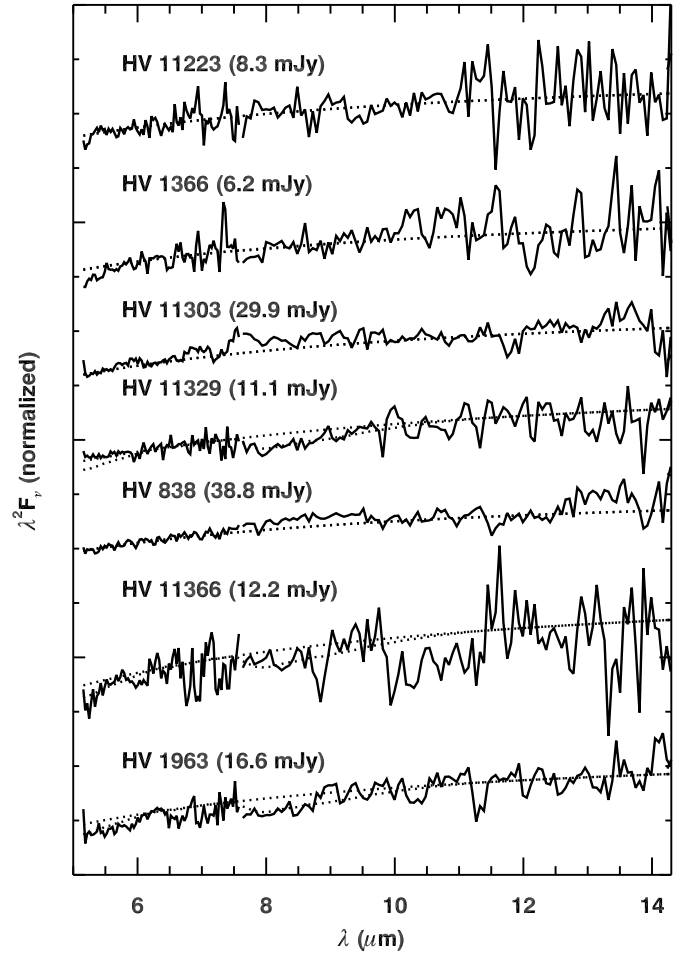


FIG. 4.— IRS spectra of naked stars in the SMC, plotted in Rayleigh-Jeans units ($\lambda^2 F_\nu$), so that the Rayleigh-Jeans tail of a blackbody would be a horizontal line. For each spectrum, the dotted lines give the fitted continuum and the best fit absorption from an average Galactic M giant. Table 6 gives the equivalent width of the fitted SiO band.

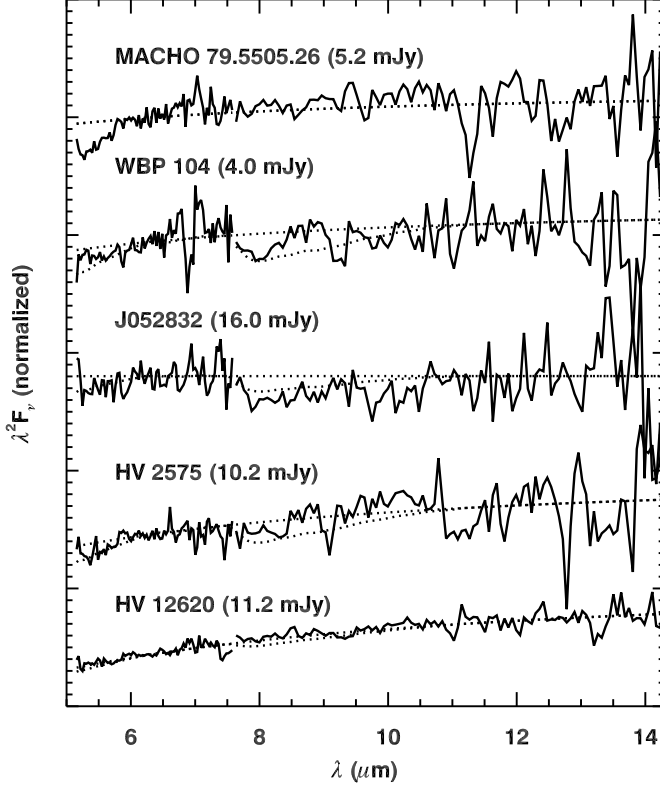


FIG. 5.— IRS spectra of naked stars in the LMC, plotted in Rayleigh-Jeans units with the fitted continuum and absorption spectra, as in Fig. 4.

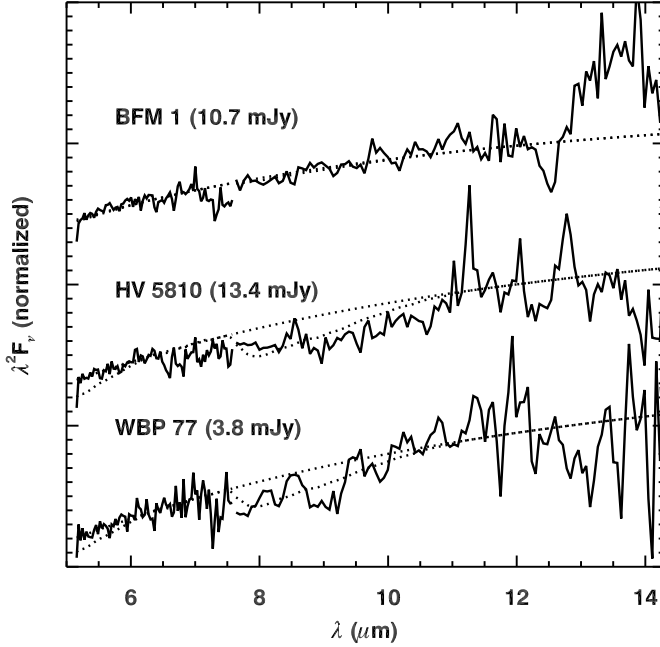


FIG. 6.— IRS spectra of stars in the SMC and LMC with indications of low-contrast dust emission (in Rayleigh-Jeans units). The dotted lines are the fitted continua and absorption spectra, as in Fig. 4. Spectra with full wavelength coverage for these sources appear in later figures: BFM 1 in Fig. 8, HV 5810 in Fig. 22, and WBP 77 in Fig. 9.

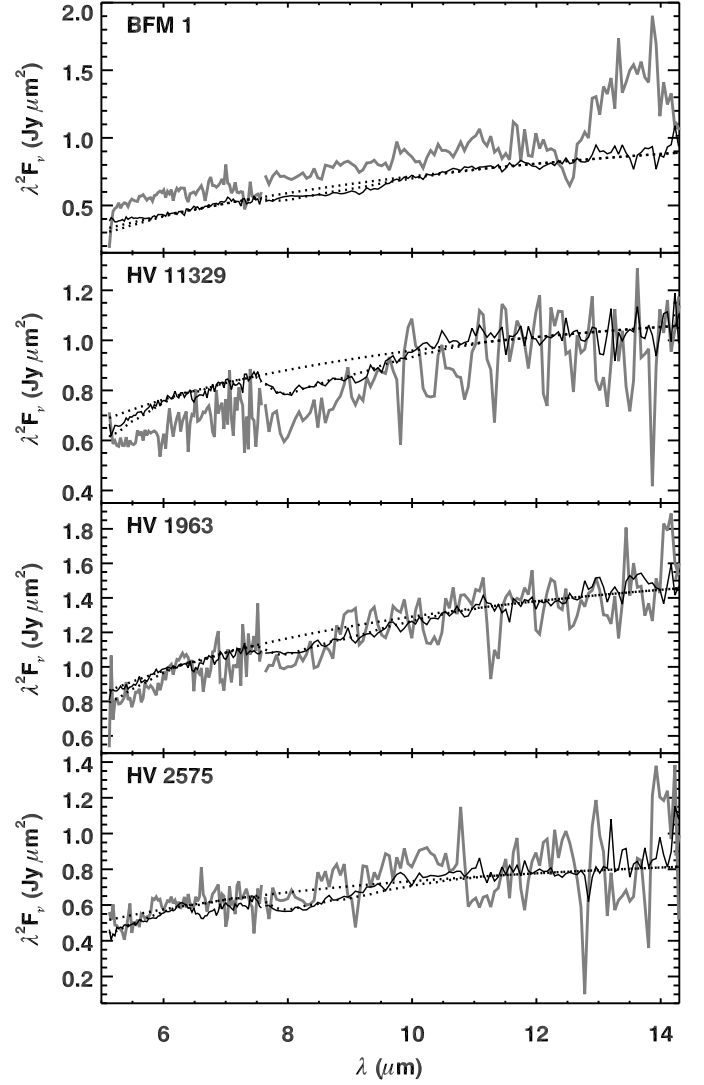


FIG. 7.— The follow-up spectra with longer integration times of four of the MC_DUST targets. The originally observed spectrum appears in light gray, while the new spectrum is in black. The dotted lines are the continuum fitted to the new spectrum and the best-fit absorption spectrum, as in Fig. 3.

the slit will be subtly distorted, since the slit throughput is a complex function of both wavelength and position in the slit (Keremdjiev & Sloan 2006). As Table 6 shows, the uncertainty in the temperature can be substantial in the noisier spectra. However, the temperatures can be useful if treated carefully. Table 6 reveals a correlation between higher dust emission contrasts and lower temperatures, suggesting that sources with lower blackbody temperatures do show low-contrast excess emission from dust.

The classifications of naked stars in Tables 3 and 6 require some clarification. If a colon follows the “N”, it indicates uncertainty about whether or not the source is naked (i.e. it is a “fig-leaf” source). If the colon follows the “O”, then the SiO band is detected with a S/N between ~ 1 and ~ 2 .

Figure 6 presents the three sources with a DEC too high to be naked and too low to identify the nature of the dust excess. BFM 1, the S star in the SMC, has a DEC of ~ 0.20 , indicating the presence of some dust. The

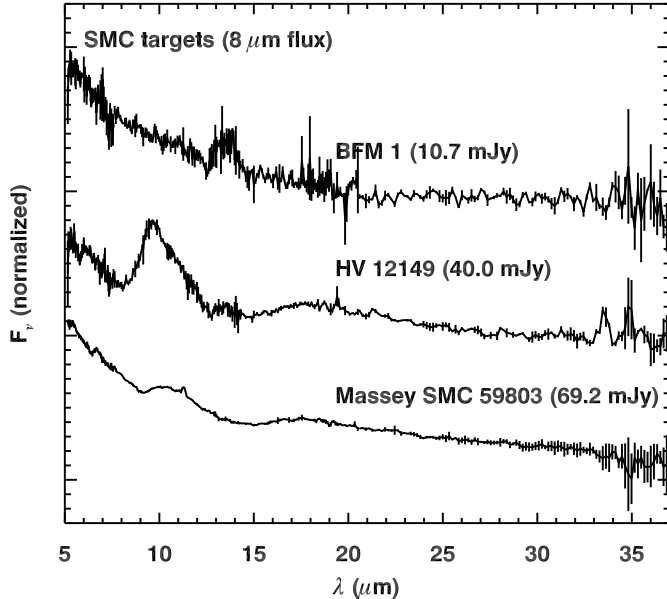


FIG. 8.— Spectra of the three SMC sources showing silicate or possibly related dust emission features.

full spectrum of this source appears in §5, along with a discussion of the interesting feature at 13–14 μm . HV 5810 shows an apparent SiO absorption feature, but it also shows apparent emission features at 11.3, 12.0, and 12.7 μm , the positions of the out-of-plane C–H bending modes in PAHs (e.g. Allamandola et al. 1989). The apparent SiO absorption is more likely just the trough between the 7–9 μm and 11–13 μm PAH complexes (despite a S/N ratio of ~ 2). This interpretation is strengthened by the spectral structure at 8.5 μm , which resembles the emission feature from the C–H in-plane bending mode in PAHs. We discuss this source further in §7.2 below.

Figure 7 presents the follow-up observations with longer integrations of four of our targets. We have detected SiO bands in all four of the follow-up spectra at a S/N of ~ 3 or better, which is an improvement over the original spectra, where the limited S/N allowed only two detections with a S/N ratio of just ~ 2 . The follow-up spectrum of BFM 1 has changed compared to the original. The apparent 13–14 μm emission feature is absent, while the SiO band is now clearly present, though weak. The S/N ratio of the spectrum of HV 2575 is high enough to reveal weak absorption between 6.5 and 7.4 μm from water vapor (Cami 2002).

We will return to the naked stars in §8.1 and 8.3 below.

5. OXYGEN-RICH DUST SOURCES

The MC_DUST sample contains 18 spectra dominated by silicate dust and related oxygen-rich dust species, as Figures 8 through 10 show. The SMC sample has three oxygen-rich dust emission sources, and no sources with enough dust opacity to drive the 10 μm feature into absorption. The LMC sample includes 12 emission sources, one red source showing a self-absorbed 10 μm silicate feature, and two even redder sources with silicate absorption at 10 μm .

5.1. Classification

The classification method introduced by Sloan & Price (1995, 1998) quickly distinguishes the composition of the

emitting oxygen-rich dust. We apply that method here, fitting an assumed photospheric spectrum to the blue end of the observed spectrum and subtracting it to isolate the dust contribution. Because the photospheric spectra in the Magellanic Clouds have weaker SiO absorption than in the Galactic sample (see §4), we depart from the previous method and simply assume a 3600 K Planck function for the star. We fit it to the spectrum in the interval 6.8–7.4 μm and subtract it. The classification is based on the ratios of the flux from the dust spectrum in small wavelength intervals centered at 10, 11, and 12 μm . Figure 11 shows that the flux ratios from oxygen-rich dust trace the *silicate dust sequence*. We classify the spectra based on their position up this sequence, starting with SE1 in the lower left and running to SE8 in the upper right. The silicate emission index = $10(F_{11}/F_{12}) - 7.5$, where F_{11}/F_{12} is the corrected ratio found by locating the point on the power law $F_{10}/F_{12} = 1.32(F_{10}/F_{11})^{1.77}$ closest to the actual value for a given spectrum. Table 7 presents the results.

We also measured the magnitude of the stars in two narrow filters (6.8–7.4 and 14.4–15.0 μm) to produce a [7]–[15] color. Table 7 includes these colors; we will examine these colors more closely when comparing other samples in a future paper.

5.2. Crystalline silicate structure beyond 20 μm

Figure 10 shows the spectra of the three most embedded sources in the MC_DUST sample, all in the LMC. Two of these sources show clear evidence of crystalline silicate emission features at 23, 28, and 34 μm . The third, IRAS 05329, shows strong fringing in LL1 that obscures the crystalline feature at 23 μm and partly hides the one at 28 μm . These crystalline features are much broader than the instrumental resolution, so a boxcar smoothing algorithm applied to LL1 will mask the fringes without significantly degrading the emission features. For IRAS 04545 and IRAS 05402, we applied a 3-pixel boxcar to all wavelengths and then applied an additional 5-pixel boxcar to the LL1 data to the blue of 22.88 μm . For IRAS 05329, with its stronger fringing pattern, we applied a 5-pixel boxcar at all wavelengths and a second 5-pixel boxcar to the blue of 30.5 μm . We stitched and trimmed these defringed spectra in the same manner as described in §3.1. Figure 12 presents the results. (Correcting the fringes changed the segment-to-segment normalization.)

We fitted a spline to the data at 20.0, 21.3, 24.5, 25.5, 31.6, and 36.5 μm to produce the spectra in Figure 13. The bottom panel in Figure 13 plots a model constructed from laboratory spectra of forsterite (Fabian et al. 2001b) and enstatite (Jäger et al. 1998), the magnesium-rich endmembers of the olivine (Mg_2SiO_4) and pyroxene (MgSiO_3) series, respectively. We have produced optical efficiencies from the published indices of refraction for a modified continuous distribution of ellipsoids which uses quadratic weighting to emphasize spherical grains (CDE2), following the methods described by Fabian et al. (2001b). We found that a grain temperature of 80 K reproduced the average relative strengths of the 23 and 34 μm features, which both arise from forsterite. In order to reproduce the strong emission feature at 28 μm , our sample had to include equal parts enstatite and forsterite. Adding enstatite also improves the match to the wavelength of the observed feature at

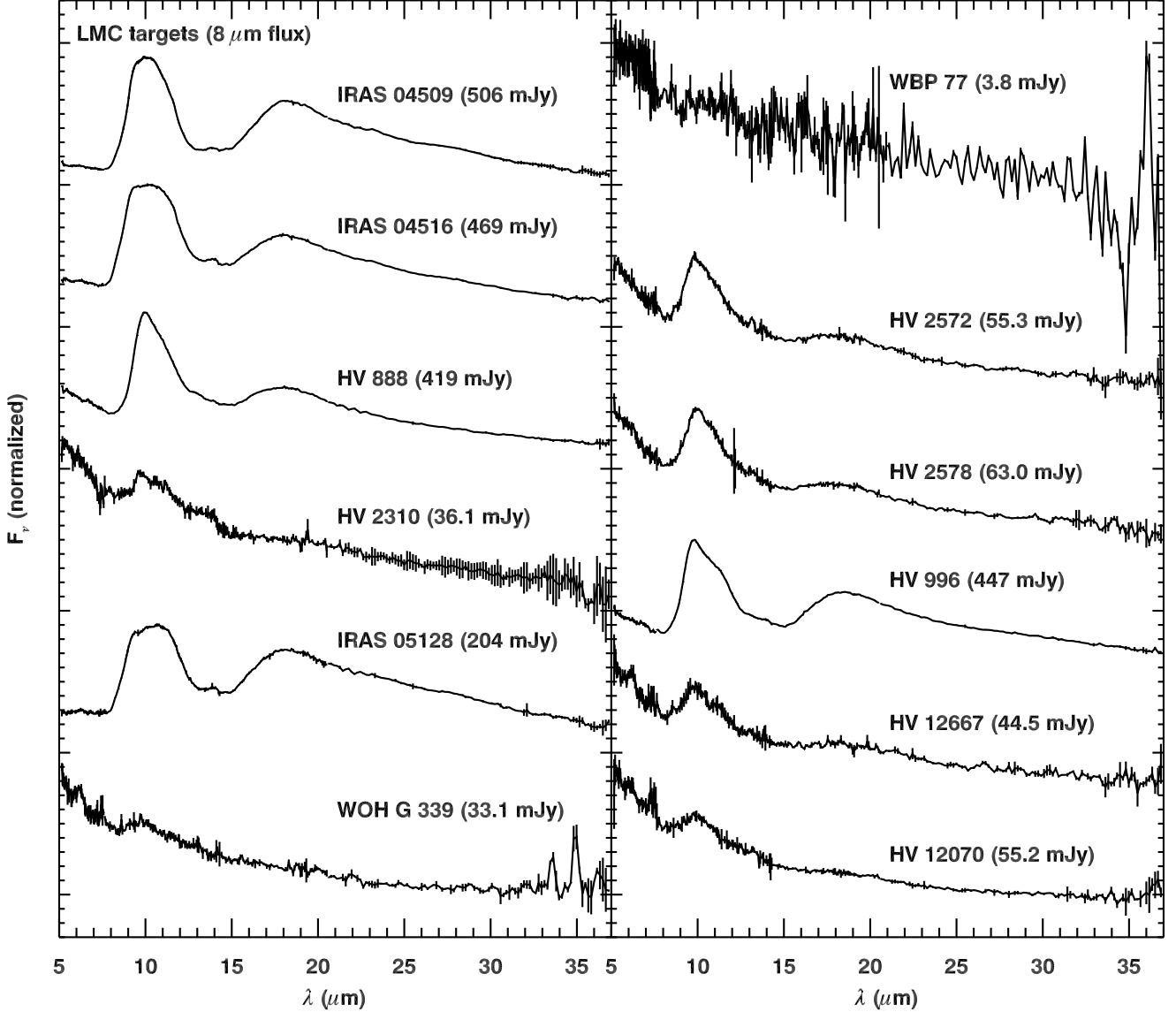


FIG. 9.— Spectra of the 12 LMC sources with silicate or related emission.

28 μm .

Spectra from the SWS on *ISO* of Galactic sources of crystalline silicates serve as a useful comparison. Molster et al. (2002) found important differences between spectra produced by objects with known disks and objects where the emitting dust was in stellar outflows, particularly at 28 and 34 μm . Their Figures 3, 4, and 5 present mean spectra from disk and outflow objects for the 23, 28, and 34 μm features, respectively. For comparison, we concentrate on IRAS 04545 and IRAS 05402 due to the higher quality of their spectra compared to IRAS 05239. In both spectra, the 23 μm feature shows a sharp peak at 23.25 μm . This differs from both the Galactic disk sources, which show a peak at 23.6 μm , and the Galactic outflow sources, which have a broader peak from 22.8 to 23.8 μm . The 28 and 34 μm features in the LMC sources both resemble the Galactic disk sources. In the LMC sources, the 28 μm feature peaks at 27.9 μm and is as strong as the 23 and 34 μm features. In the Galactic samples, the 28 μm feature is largely absent in

the outflow sources, but strong in the disk sources.¹² In the LMC sources, the 34 μm feature peaks at 33.7 μm , as does the Galactic disk sample, while the Galactic outflow sample shows an additional peak at 32.9 μm which appears as only a shoulder in the disk spectra. Thus, while the 23 μm feature differs somewhat from the Galactic sample, both the 28 and 34 μm features closely resemble spectra from Galactic sources of crystalline silicates, especially those found in circumstellar disks.

Several effects can shift the wavelength of the observed features. Suto et al. (2006) recently investigated how the emission features from forsterite shift with temperature. Using their data, we could expect a shift to the red of 0.21 μm in the 23.25 μm feature, 0.25 μm at 27.9 μm , and 0.22 μm at 33.7 μm if we were to heat the grains in our observed spectra from 80 K to 300 K, which is the

¹² The spectra produced by Molster et al. (2002) show additional structure at ~ 29.5 and 30.5 μm , but this spectral region is notoriously difficult in the SWS data, due to problems in spectral bands 3D and 3E, making this structure questionable (Sloan et al. 2003, discuss this in more detail).

TABLE 7
SILICATE EMISSION ANALYSIS

Target	[7]–[15]	Dust Em. Contrast	F_{10}/F_{11}	F_{10}/F_{12}	Corrected F_{10}/F_{11}	Infrared Sp. Class
BFM 1	0.41±0.07	0.24±0.04	2.ST
BFM 1 (follow-up)	0.62±0.06	0.16±0.02	2.NO
HV 12149	0.88±0.02	0.80±0.04	1.39±0.05	2.29±0.13	1.68±0.11	SE8
Massey SMC 59803	0.58±0.01	0.23±0.01	0.77±0.03	1.08±0.04	1.19±0.06	SE4
IRAS 04509	2.12±0.01	3.96±0.05	1.17±0.02	2.06±0.07	1.59±0.06	SE8
IRAS 04516	2.00±0.01	3.22±0.02	1.02±0.01	1.47±0.04	1.38±0.04	SE6
IRAS 04545	2.22±0.01	1.51±0.01	3.SA
HV 888	1.60±0.01	1.90±0.01	1.27±0.02	2.00±0.05	1.58±0.05	SE8
HV 2310	0.88±0.03	0.63±0.02	1.00±0.04	1.26±0.02	1.30±0.05	SE5
IRAS 05128	1.93±0.00	2.42±0.02	0.95±0.01	1.25±0.02	1.29±0.03	SE5
HV 5810	1.02±0.02	0.19±0.08	2.U
WOH G 339	0.92±0.02	0.46±0.02	1.11±0.04	1.14±0.06	1.27±0.08	SE5
WBP 77	1.01±0.10	0.19±0.07	0.72±0.14	0.43±0.10	0.88±0.26	SE1:
HV 2572	1.06±0.01	0.80±0.02	1.23±0.02	1.73±0.03	1.49±0.03	SE7
HV 2578	1.05±0.01	0.85±0.03	1.24±0.03	1.85±0.06	1.53±0.06	SE7
HV 996	1.63±0.01	1.88±0.01	1.19±0.01	1.65±0.04	1.46±0.04	SE7
IRAS 05329	1.94±0.00	1.14±0.03	3.SB
IRAS 05402	2.24±0.00	2.29±0.04	3.SA
HV 12667	0.92±0.01	0.57±0.03	1.17±0.02	1.54±0.06	1.42±0.06	SE6
HV 12070	0.60±0.02	0.29±0.02	1.16±0.01	1.50±0.02	1.41±0.03	SE6

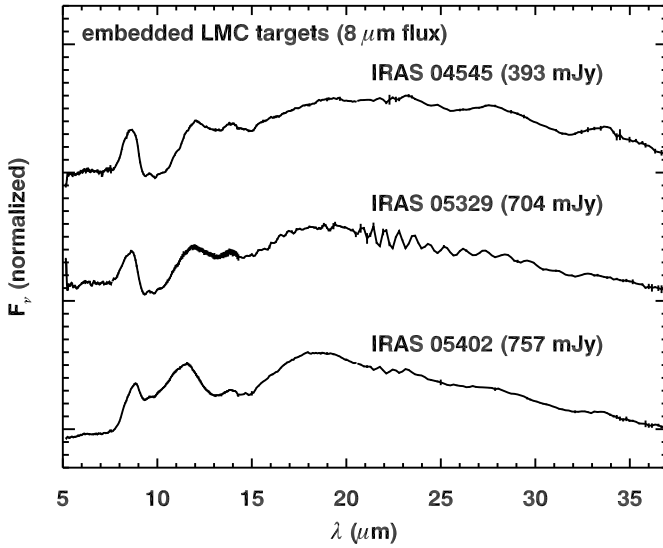


FIG. 10.— Spectra of the three LMC sources showing silicate absorption features or self-absorbed silicate features at 10 μm . These spectra are analyzed in Fig. 12 and 13.

temperature of the measured laboratory samples. The bottom panel of Figure 13 includes vertical dotted lines illustrating these shifts.

Another way to shift the features is to replace some of the Mg in the minerals with Fe. Chihara et al. (2002) and Koike et al. (2003) studied this effect in pyroxenes and olivines, respectively. In pyroxenes, replacing 20% of the Mg with Fe shifts the 28 μm feature by 0.4 μm , while a similar replacement in olivines shifts the 23 μm feature 0.3 μm and the 34 μm feature 0.2 μm .

The shape of the grains also influences the wavelengths of the emission features, as Min et al. (2003) have thoroughly investigated. Generally, a shift from spherical to non-spherical shape distributions moves the features to longer wavelengths. Most examinations of this effect have assumed that no particular axis is favorably extended in a sample of grains. Sloan et al. (2006a) exam-

ined the effect of preferential non-sphericity along different axes and found that some shapes could shift the features to the blue, instead of the red.

The solid vertical lines in Figure 13 mark the average peaks of the features in IRAS 04545 and IRAS 05402. In the bottom panel, we should compare the peaks of the model spectrum to the *dotted* vertical lines, since these account for the difference in temperature between the laboratory and LMC data. The observed position of the 23 μm forsterite feature shows no redshift compared to the laboratory data, indicating Mg-rich grains with a CDE2 shape distribution are a good fit. The 28 μm feature, which arises from a mixture of enstatite and forsterite, is $\sim 0.3 \mu\text{m}$ to the red of the laboratory data, indicating Fe inclusions of no more than $\sim 15\%$ or a slightly different shape distribution. Less can be said about the relative positions of the 34 μm feature in the observed and laboratory data because of the clear difference in profile. Overall, our observations of crystalline silicates in the LMC are fully consistent with Mg-dominated grains, much like those observed in the Galaxy.

5.3. Crystalline silicate structure at 10 μm

Sloan et al. (2006a) published the spectrum of HV 2310, one of the first objects observed in the MC_DUST program. This 600-day Mira shows an unusual silicate emission spectrum with structure in the 10–11 μm region best fit with a mixture of 7% crystalline forsterite and a blend of amorphous grains dominated by astronomical silicates (as described by Ossenkopf et al. 1992). They based their analysis on S11 pipeline output from the SSC, while the data here are S15. While the general shape is still indicative of crystalline silicates, the spectral details have changed enough to require a new analysis.

The MC_DUST sample has revealed one more object showing crystalline silicate structure at 10 μm , HV 12667. This source is a 645-day Mira, so it has similar pulsation properties to HV 2310, and it also has a similar infrared brightness, 45 mJy at 8 μm , compared to 36

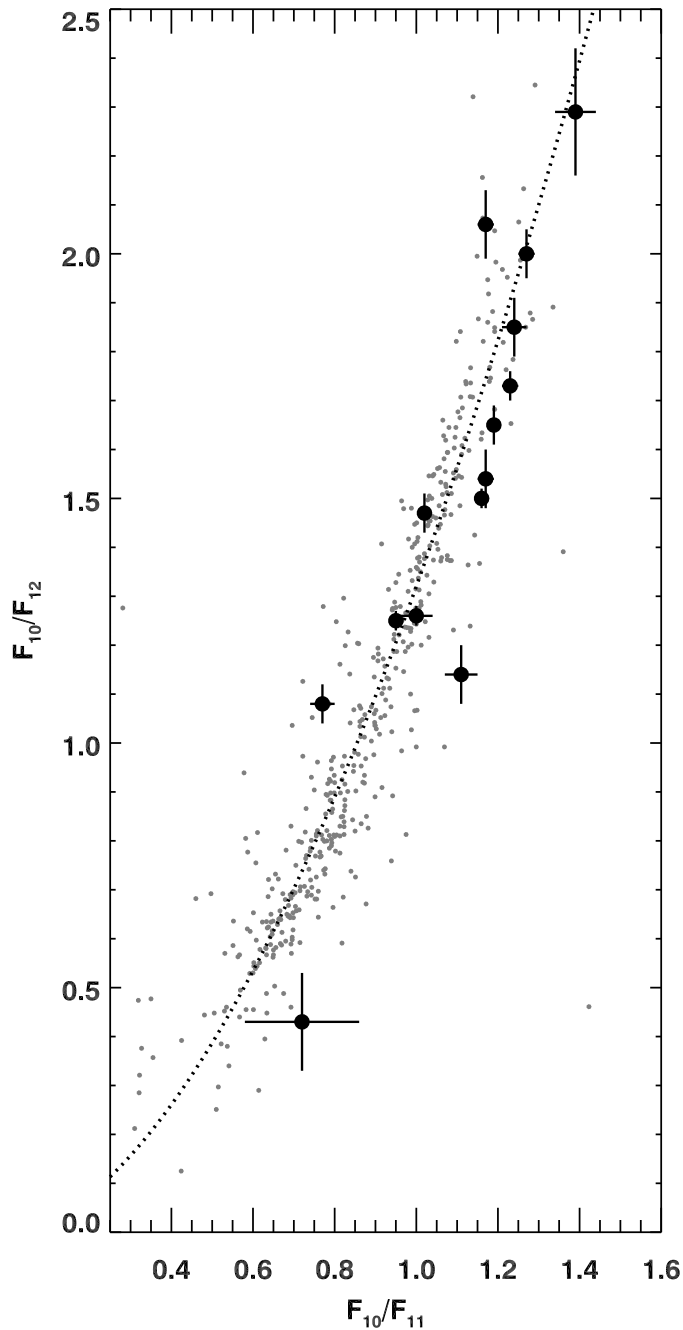


FIG. 11.— The silicate dust sequence. MC_DUST sources are plotted with black filled circles. The smaller gray circles show the distribution of Galactic AGB sources (Sloan & Price 1995, 1998), and the dotted curve is a power law: $F_{10}/F_{12} = 1.32(F_{10}/F_{11})^{1.77}$.

mJy for HV 2310.

Figure 14 plots the continuum-subtracted spectra of HV 2310 and HV 12667. In both cases, we have fitted and subtracted a 3600 K Planck function at 5.3–5.8 μm . We tested the dependency of our results on the assumed stellar continuum by also using a model M6 giant with SiO absorption at 8 μm , and we found no significant impact. Figure 14 also includes a rough fit to the dust spectrum, using a combination of amorphous silicates (Ossenkopf et al. 1992) and forsterite (Jäger et al. 1998). Following Sloan et al. (2006a), we have produced a modified shape distribution in an effort to reproduce the de-

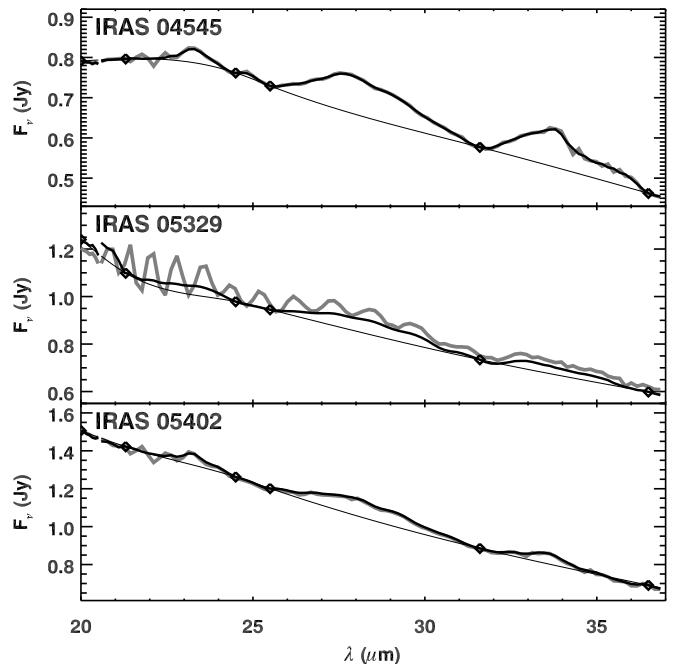


FIG. 12.— The crystalline silicate emission features apparent in three LL spectra. The data plotted in gray are the original spectra, while the data plotted in black are the spectra which have been defringed by boxcar smoothing, as explained in the text. The thin black line is the spline fitted at wavelengths marked by diamonds. Fig. 13 presents the resulting crystalline silicate spectra.

tailed structure of the 10 μm silicate feature. In the case of HV 12667, we have used a distribution of spherical grains, and prolate grains extended along the x axis. To fit the observed spectrum, this population of crystalline grains needs to account for 2.5% of the dust; the rest is amorphous silicates. For HV 2310, the shape distribution includes prolate grains (x axis) and oblate grains (x and z axes). The crystalline component of the dust population is 7%, unchanged from before. Sloan et al. (2006a) also included amorphous pyroxene and amorphous alumina to fit the blue and red wings of the silicate profile, respectively. We do not include these components because we wish to concentrate on the structure at the peak of the profile.

It is highly unlikely that these shape distributions fit the silicate profiles uniquely. In fact, the changes in the pipeline calibration have changed the spectrum of HV 2310 enough that we have modified the shape distribution used by Sloan et al. (2006a). The prolate grains in their shape distribution were extended along the z axis, vs. the x axis here. This difference illustrates that the data are not of sufficient fidelity to pin these details down. However, the fits to HV 2310 and HV 12667 demonstrate that the silicate profiles in both are consistent with forsterite and that it is not necessary to invoke enstatite or minerals with Fe components to fit the features.

5.4. The 13 μm emission feature

The 13 μm emission feature, first detected by Little-Marenin & Price (1986), often appears in the spectra from Galactic oxygen-rich dust shells (Sloan et al. 1996). In our Magellanic samples, it is largely absent. There may be a feature in the spectra of HV 2572 and HV 2578, but if so, it is weak, noisy, and difficult to mea-

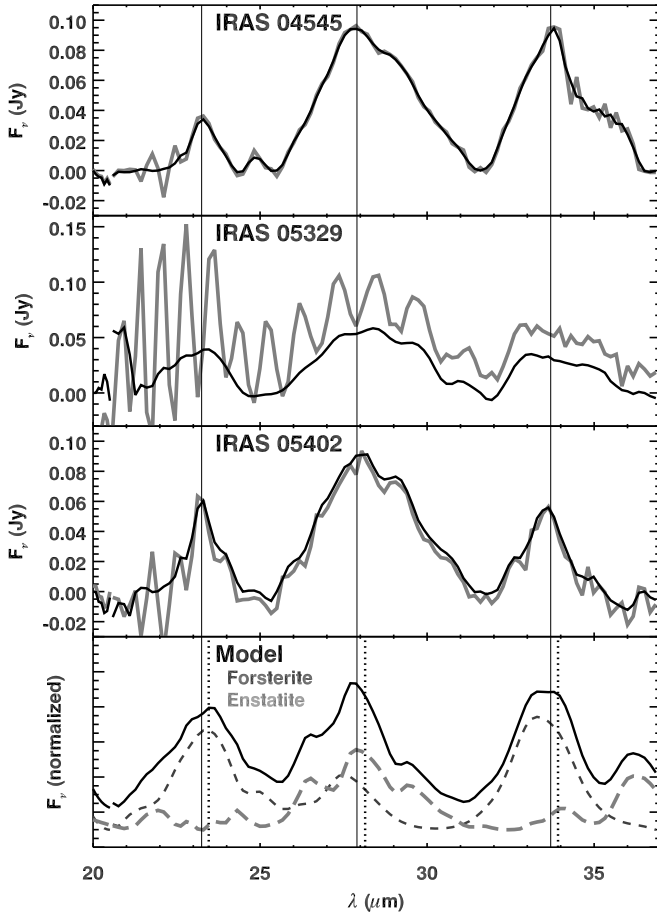


FIG. 13.— The spline-subtracted crystalline silicate emission features from the spectra in Fig. 12. In the top three panels, the smoothed data are in black and the unsmoothed data are in light gray. The vertical lines mark reference wavelengths at 23.25, 27.9, and 33.7 μm . The bottom panel presents a model spectrum (black) composed of 50% laboratory forsterite (Mg_2SiO_4 , dark gray; Fabian et al. 2001b) and 50% laboratory enstatite (MgSiO_3 , light gray; Jäger et al. 1998), both at 80 K and assuming a CDE2 shape distribution (see text). The vertical dotted lines in the bottom panel illustrate how the observed peaks should shift from 80 K to 300 K, based on the laboratory work by Suto et al. (2006).

sure. The spectra of IRAS 04509, IRAS 04516, and IRAS 05128 show features in this spectral region, but they are centered closer to 14 μm , as discussed in the next section.

Our sample of oxygen-rich dust spectra is small, it may contain some biases (e.g. for Mira variables, which are less likely to show a 13 μm feature than semiregular variables), and some of the spectra are noisy, which can hide low-contrast emission features. Consequently, our conclusion that the prevalence and strength of the 13 μm emission feature is reduced in the Magellanic Clouds is somewhat preliminary. A more thorough examination of oxygen-rich circumstellar dust observed in other Magellanic programs is in preparation.

5.5. The 14 μm emission feature

Sloan et al. (2006a) previously noted that the spectrum of HV 2310 includes an emission feature at 14 μm . They were somewhat cautious about the feature, since it appears at the boundary between SL and LL, raising the possibility that it is an artifact, even if no known effect in the IRS could produce such a feature. Emery et al. (2006) also detected a 14 μm emission feature in the

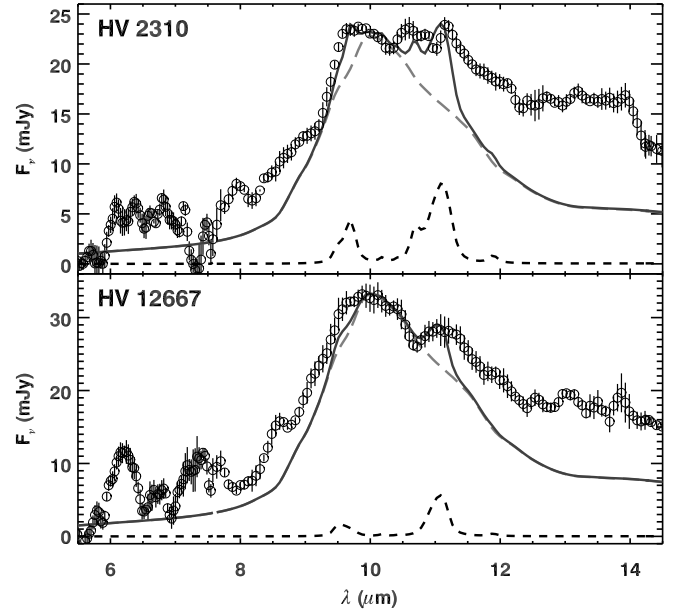


FIG. 14.— Structured silicate emission at 10 μm in HV 2310 (top) and HV 12667 (bottom). The IRS data (circles and error bars) have been smoothed with a 3-pixel boxcar. The fitted model dust spectrum (solid black line) is a combination of amorphous silicates (dashed gray curve; Ossenkopf et al. 1992) and forsterite (Mg_2SiO_4 ; dashed black curve; Fabian et al. 2001b). For HV 2310, 7% of the grains are crystalline, with a shape distribution including spherical, prolate (along the x axis), and oblate (extended along the x and z axes). For HV 12667, 2.5% of the dust is crystalline, and the shape distribution includes spherical grains and prolate grains (x axis).

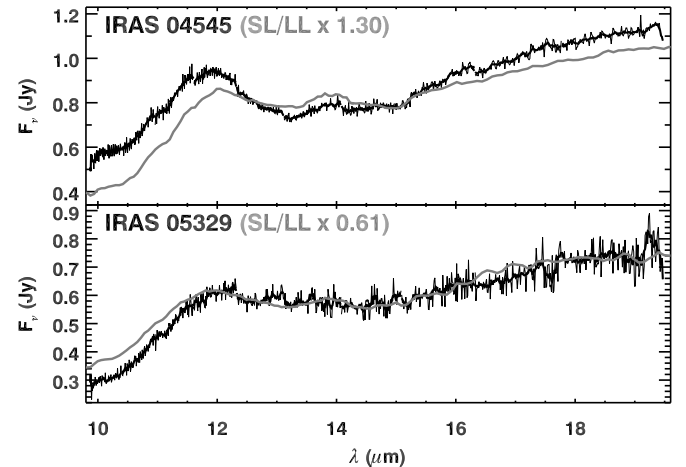


FIG. 15.— The 14 μm feature in IRAS 04545 (top) and IRAS 05239 (bottom), in low-resolution IRS data (light gray) and SH data. The SH spectra are plotted before and after smoothing with a 7-pixel boxcar. IRAS 04545 increased 30% in brightness, producing a high-quality SH spectrum which confirms the presence of the 14 μm feature. IRAS 05239, on the other hand, dimmed by 40%, making confirmation more difficult.

IRS spectra of the Trojan asteroids 624 Hektor and 921 Agamemnon, but they were also cautious and did not suggest a possible carrier. Figures 9–10 reveal that several sources in the MC_DUST sample besides HV 2310 also have 14 μm features.

To test if the feature might be an artifact in the low-resolution IRS spectra, we observed two 14 μm sources, IRAS 04545 and IRAS 05239, with the SH module, as shown in Figure 15. Both sources are variable stars, and

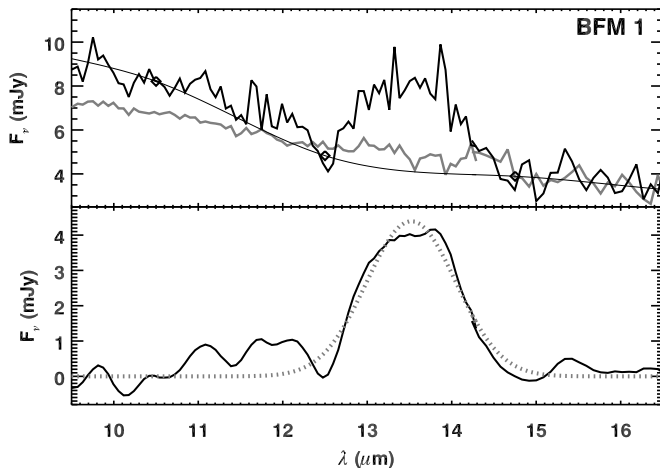


FIG. 16.— The spectrum of BFM 1 from 9.5 to 16.5 μm , as originally observed (in black), and when followed up with a longer integration time (in gray) 418 days later. The thin black curve is a spline fitted through the original spectrum to isolate the possible dust spectrum shown in the bottom panel. In the bottom panel, the spectrum has been smoothed, and the fitted Gaussian (dashed gray curve) is centered at 13.52 μm and has a FWHM of 0.53 μm .

IRAS 04545 increased in brightness by 30% between the two observations, resulting in an excellent SH spectrum which clearly confirms the detection in SL and LL. IRAS 05329 declined in brightness by nearly 40%, and as a consequence, the SH spectrum is noisier. While the SH data are consistent with the low-resolution data, they do not show an obvious 14 μm feature.

5.6. BFM 1

As shown in Figures 6, 7, and 8, BFM 1 has some unusual spectral characteristics. First, while the spectrum shows no substantial structure out to 12.5 μm , it has a significant dust emission contrast (0.24 when first observed, and 0.16 when followed up), indicating the presence of a featureless excess component. Second, the original spectrum shows a previously unknown emission feature from 13 to 14 μm . Third, the follow-up spectrum, taken 418 days later with a longer integration time, confirms the featureless dust excess, but shows nothing where the 13–14 μm feature had previously been.

BFM 1 is the only true S star in our sample, and it is a steady Mira variable with a 398-day period and an amplitude of about 4 magnitudes in the optical. In S stars, the C/O ratio is near unity, leaving little C or O for the production of dust once CO has formed, which could lead to unusual dust chemistry. Our spectra of BFM 1 certainly show unusual characteristics. The featureless excess is not consistent with amorphous alumina, as that would leave a recognizable low-contrast feature in the 11–12 μm region. Perhaps it is amorphous carbon, or some other dust component.

The possible feature at 13–14 μm is also enigmatic. The follow-up spectrum did not confirm its presence, so either it disappeared in the interval between the observations, or else it was an artifact to begin with. The two spectra were obtained 418 days apart, compared to the 398-day period of the star. Thus the spectra were at nearly the same phase, ruling out some phase-dependent phenomenon. Nonetheless, we suspect the feature is real. First, it appears in the spectra from both nod positions. Second, it covers over 25 pixels in SL and is not the prod-

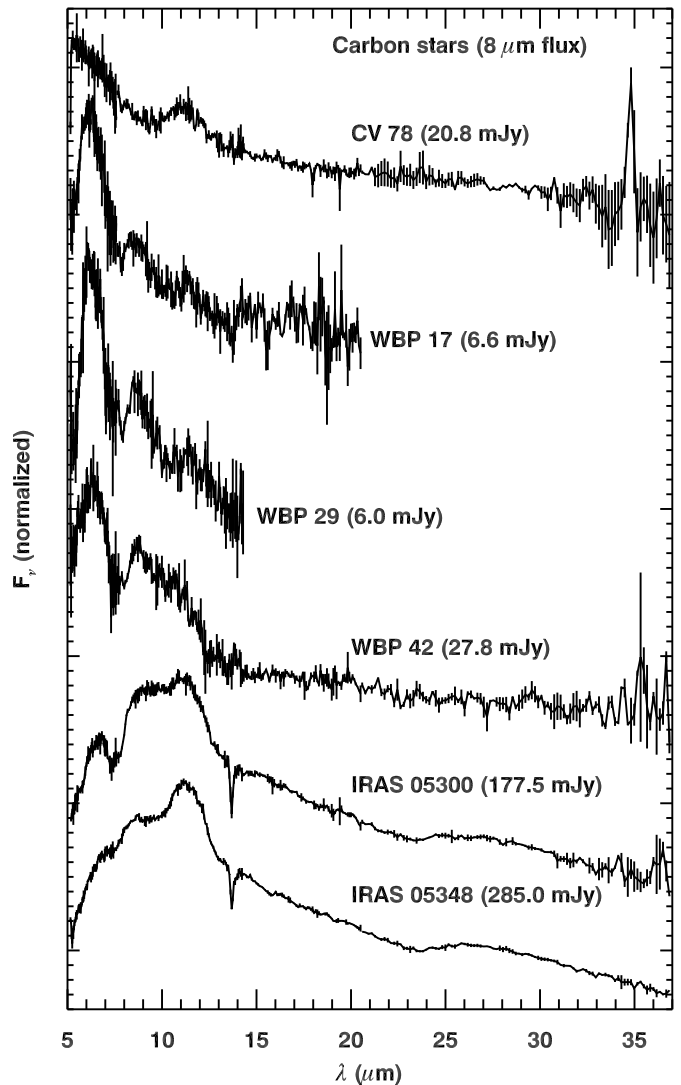


FIG. 17.— The six definite carbon stars in the MC_DUST sample. CV 78, the top spectrum, is in the SMC; the rest are in the LMC. The spectra of WBP 17 and WBP 29 are truncated at longer wavelengths due to background issues. The spectrum of a seventh source, MACHO 79.5505.26, appears in Fig. 2 and 4 and has an uncertain chemistry.

uct of any known artifact. Third, similar features appear in two of the 90 spectra in the sample of Galactic S stars observed by the IRS in Cycle 3 (Sloan et al. 2008b, Program ID 30737, P.I. S. Hony).

Figure 16 focuses on the 13–14 μm feature in BFM 1. Fitting a spline to remove the continuum isolates a feature which can be fit with a Gaussian centered at 13.52 μm with a full width at half maximum (FWHM) of 0.53 μm . The unique spectrum of BFM 1 deserves a unique classification. We extend the Hanscom system with a new classification, 2.ST, where the “T” indicates a feature centered at 13.5 μm .

6. CARBON-RICH SOURCES

The MC_DUST sample includes one definite carbon star in the SMC and five in the LMC. Figure 17 presents the spectra of these sources. In addition, MACHO 79.5505.26 has a carbon-rich optical spectrum but an ambiguous infrared spectrum with no dust emission and only CO absorption at 5 μm . Its spectrum appears in

Figures 2 and 4. In the next section, we show that it has no carbon-rich absorption features. We exclude it from further analysis as a carbon star because the chemistry of the infrared component is uncertain.

We have truncated the spectra of two sources in Figure 17 to avoid some problems introduced by complex backgrounds. The LL1 data for WBP 17 are negative due to strong background gradients. A nearby bright carbon star contaminates the LL data for WBP 29.

6.1. The Manchester Method

To analyze the carbon-rich spectra, we applied the Manchester method introduced by Sloan et al. (2006b) and also applied by Zijlstra et al. (2006) and Lagadec et al. (2007). These papers examined a total of 28 carbon stars in the LMC and 33 in the SMC, while our sample adds five carbon stars in the LMC and one in the SMC. The Manchester method measures the spectral continuum at four narrow wavelength intervals relatively free of molecular band absorption or dust emission centered at 6.3, 9.4, 16.5, and 21.5 μm . The first two wavelengths define the [6.4]–[9.3] color, which measures the contribution from warm dust relative to the stellar photosphere. The [16.5]–[21.5] color measures the temperature of any cool dust contribution to the spectrum. It also provides a means of estimating the contribution under the MgS dust emission feature, which peaks in the 26–30 μm range.

Gaseous acetylene (C_2H_2) produces two absorption bands visible in the IRS spectra: a broad band centered at 7.5 μm and typically $\sim 1.0 \mu\text{m}$ wide, and a narrow band at 13.7 μm (Matsuura et al. 2006). This latter band is actually the Q branch of the fundamental ν_5 mode and it is often centered in a broader band which includes the P and R branches, but the broad component can be difficult to recognize due to the presence of the SiC dust emission feature at 11.3 μm .

The Manchester method fits line segments to the continuum to measure the equivalent width of the acetylene bands and the integrated flux of the SiC emission feature. We express the flux of the SiC band as a ratio to the continuum underneath. To measure the strength of the MgS the Manchester method uses the [16.5]–[21.5] color to extrapolate a cool blackbody continuum beneath the feature, which peaks in the 26–30 μm range. Table 8 presents the results.

6.2. Results

Figures 18 and 19 plot the results for our sample (large symbols), along with the LMC sample of Zijlstra et al. (2006), the SMC samples of Sloan et al. (2006b) and Lagadec et al. (2007), and the Galactic sample observed by the SWS on *ISO*. The Galactic sample is defined by the carbon-rich classifications of Kraemer et al. (2002) and uses the data in the SWS Atlas (Sloan et al. 2003). The small MC_DUST sample follows the trends set by the larger samples of Magellanic carbon stars previously published. As metallicity decreases, stars with similar [6.3]–[9.4] colors show increasing absorption from acetylene and reduced emission from SiC and MgS dust.

The strength of the 7.5 μm acetylene band increases as the stars go from a [6.4]–[9.3] color of 0.0 to ~ 0.3 and then decreases as the amorphous carbon component becomes more dominant, although the scatter at a

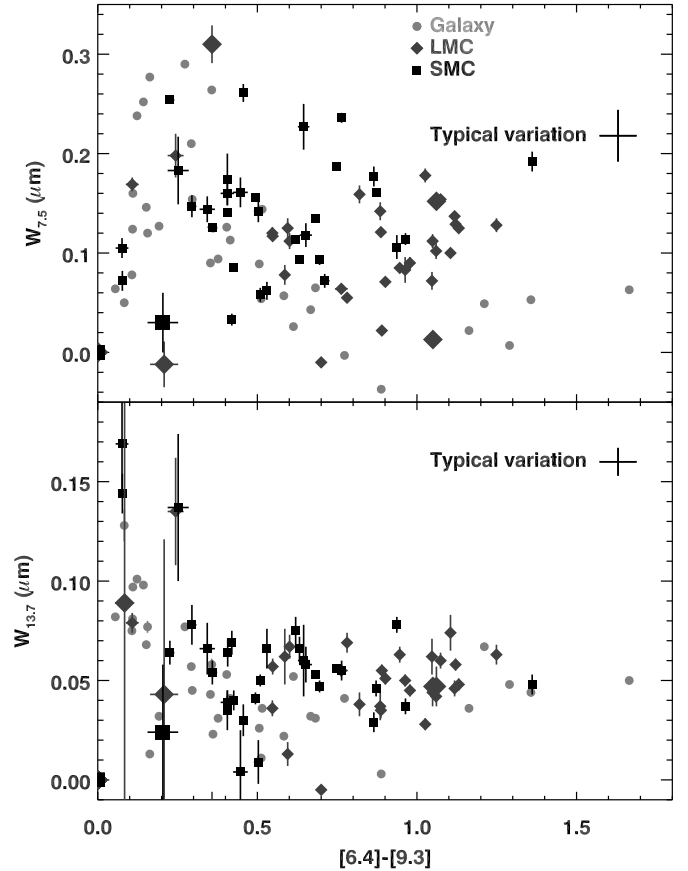


FIG. 18.— The equivalent widths of the acetylene absorption bands at 7.5 μm (top) and 13.7 μm (bottom), plotted vs. [6.4]–[9.3] color, which measures the strength of the amorphous carbon component. Galactic data are plotted with light gray circles, LMC data in dark gray diamonds, and SMC data in black squares. The MC_DUST sample are plotted with large symbols, while small symbols are from previously published samples.

given color is large. The data appear to follow two separate tracks, but the significance is not clear with these sample sizes. The strength of the 13.7 μm band generally decreases steadily from 0.10 μm to $\sim 0.05 \mu\text{m}$ at a [6.4]–[9.3] color of 0.5 and remains roughly constant beyond. In both cases, the LMC and SMC sources usually have deeper bands compared to the Galactic sources of the same color, but no clear difference between the LMC and SMC is discernable.

The strength of the SiC feature follows two distinct tracks with [6.4]–[9.3] color. The lower track starts with no SiC feature at a color of 0.0 and slowly increases to a $\sim 10\%$ strength at a color of 1.0. The upper track climbs to a $\sim 30\%$ strength at a color of ~ 0.45 , then drops to meet the lower track at redder colors. Sloan et al. (2006b) noted that five of their carbon stars in the SMC had enhanced SiC strength compared to the rest: MSX SMC 054, 091, 105, 159, and 163. In Figure 19, these five clearly fall on the upper track, which includes nearly all of the Galactic sources. Sloan et al. (2006b) were unable to find any other property that distinguished them from the rest of the SMC sample, except that they were more likely to show MgS emission. Additional SMC sources on the upper track include GM 780 from the sample of Lagadec et al. (2007) and CV 78 from the MC_DUST sample. Lagadec et al. (2007) noted that GM 780 was

TABLE 8
CARBON STAR ANALYSIS

Target	[6.4]–[9.3] (mag)	[16.5]–[21.5] (mag)	7.5 μ m EW (μ m)	13.7 μ m EW (μ m)	λ_{SiC} (μ m)	SiC/Cont.	MgS/Cont.	Infrared Sp. Class
CV 78	0.204 \pm 0.048	0.178 \pm 0.061	0.030 \pm 0.030	0.024 \pm 0.034	11.12 \pm 0.15	0.197 \pm 0.019	...	2.CE
MACHO 79.5505.26	0.208 \pm 0.044	–0.307 \pm 0.350	1.N
WBP 17	–0.113 \pm 0.047	–1.027 \pm 0.770	0.304 \pm 0.014	0.157 \pm 0.032	11.43 \pm 0.39	0.092 \pm 0.031	...	1.NC
WBP 29	0.084 \pm 0.030	...	0.395 \pm 0.011	...	12.01 \pm 0.69	0.035 \pm 0.037	...	2.CE
WBP 42	0.358 \pm 0.017	0.140 \pm 0.094	0.310 \pm 0.019	...	10.95 \pm 0.31	0.092 \pm 0.025	...	2.CE:
IRAS 05300	1.061 \pm 0.006	0.280 \pm 0.011	0.152 \pm 0.003	0.047 \pm 0.010	11.32 \pm 0.08	0.098 \pm 0.005	0.255 \pm 0.014	3.CR
IRAS 05348	1.050 \pm 0.006	0.295 \pm 0.010	0.013 \pm 0.004	0.047 \pm 0.001	11.28 \pm 0.05	0.137 \pm 0.004	0.238 \pm 0.012	3.CR

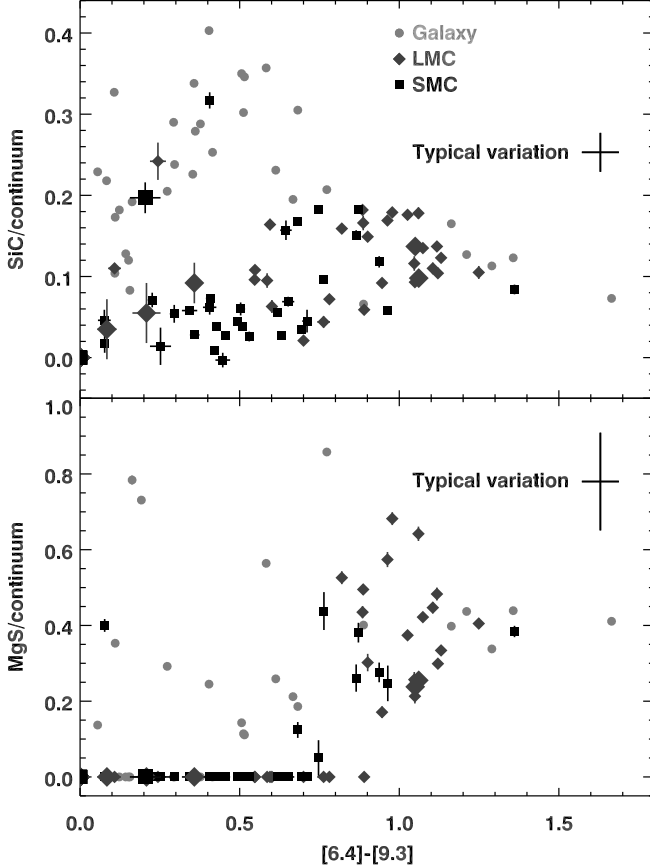


FIG. 19.— The integrated fluxes of the SiC (top) and MgS (bottom) dust features, divided by the underlying continuum and plotted as a function of [6.4]–[9.3] color. Symbols are as defined in Fig. 18.

peculiar, with no acetylene absorption and a relatively high luminosity. They argued that its C/O ratio was lower than most of the Magellanic sources and more like Galactic carbon stars, which might affect the fraction of SiC in its outflows.

The MgS strength in the SMC and LMC samples are similar to each other. Few sources bluer than [6.4]–[9.3] ~ 0.7 having any measurable MgS dust, while most Galactic sources do. At redder colors, the three samples behave similarly, with MgS strengths typically $\sim 40\%$ of the continuum, but with considerable scatter, especially in the LMC sample.

6.3. Distance indicators

Figure 20 plots the absolute magnitude at K vs. the J–K 2MASS colors for the carbon stars in the SMC sam-

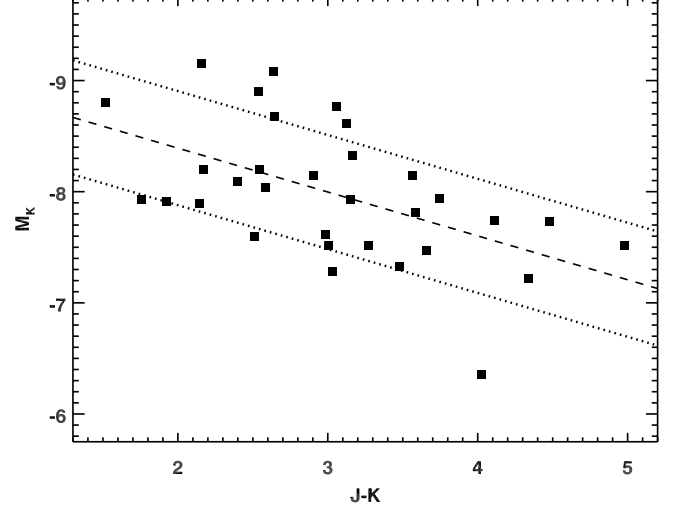


FIG. 20.— A near-infrared color-magnitude diagram for the carbon stars in the SMC samples of Sloan et al. (2006b) and Lagadec et al. (2007). The dashed line shows a line fit to the SMC data while the dotted lines show the standard deviation of the scatter about that line.

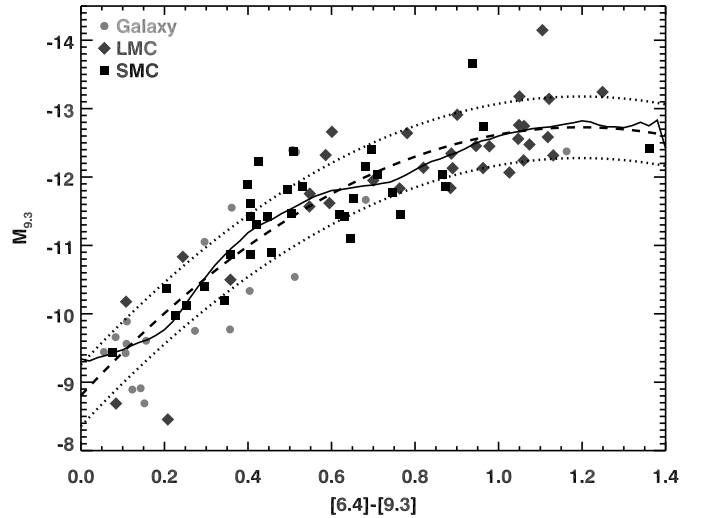


FIG. 21.— A mid-infrared color-magnitude diagram for the Magellanic and Galactic carbon stars examined by Sloan et al. (2006b), Zijlstra et al. (2006), and Lagadec et al. (2007). The solid line shows the running mean of the data as a function of [6.4]–[9.3] color. The dashed line is a quadratic fit to the data, with the dotted lines above and below showing the (smoothed) standard deviation.

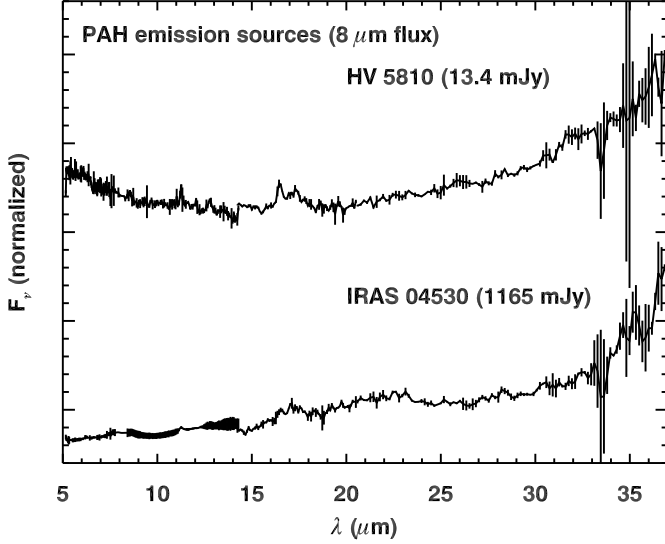


FIG. 22.— Spectra of the two red sources in the MC.DUST sample. Both show PAH emission features. A third spectrum with PAH features, of Massey SMC 59803, appears in Fig. 8.

ples of Sloan et al. (2006b) and Lagadec et al. (2007). We have assumed a distance modulus of 18.93 to the SMC (Keller & Wood 2006). The data follow a linear relation with a standard deviation of 0.51 magnitudes:

$$M_K = -9.18 + 0.395(J - K). \quad (1)$$

Applying the synthetic photometry to the spectra to generate magnitudes at 6.4 and 9.3 μm reveals a second infrared color-magnitude relation. Figure 21 plots the absolute magnitude at 9.3 μm as a function of $[6.4] - [9.3]$ color for the samples of carbon stars in the Galaxy and both Magellanic Clouds of Sloan et al. (2006b), Zijlstra et al. (2006), and Lagadec et al. (2007). The magnitudes at 9.3 μm are based on a flux density at zero magnitudes of 45.7 Jy and distance moduli to the LMC and SMC of 18.54 and 18.93, respectively (Keller & Wood 2006). The Galactic sample were observed with the SWS on *ISO*, as described by Sloan et al. (2006b). The distances were estimated by Bergeat & Chevallerier (2005). Here, the relation is quadratic:

$$M_{9.3 \mu\text{m}} = \Sigma a_i ([6.4] - [9.3])^i, \quad (2)$$

where $a_0 = -8.81$, $a_1 = -6.56$, and $a_2 = 2.74$. The standard deviation of the data about this relation is 0.45 magnitudes.

7. PAH EMISSION SOURCES

Figure 22 presents the spectra of the two red sources in the MC.DUST sample, IRAS 04530 and HV 5810. Both of these spectra have PAH emission features. A third source, the supergiant Massey SMC 59803, also shows PAH emission superimposed on an oxygen-rich dust spectrum. Its spectrum appears in Figure 8.

Figure 23 includes 8 and 24 μm images of the three PAH emission sources. The data for Massey SMC 59803 were obtained as part of the S³MC survey by Bolatto et al. (2007). Data for the other two sources are from the SAGE survey (Meikle et al. 2007).

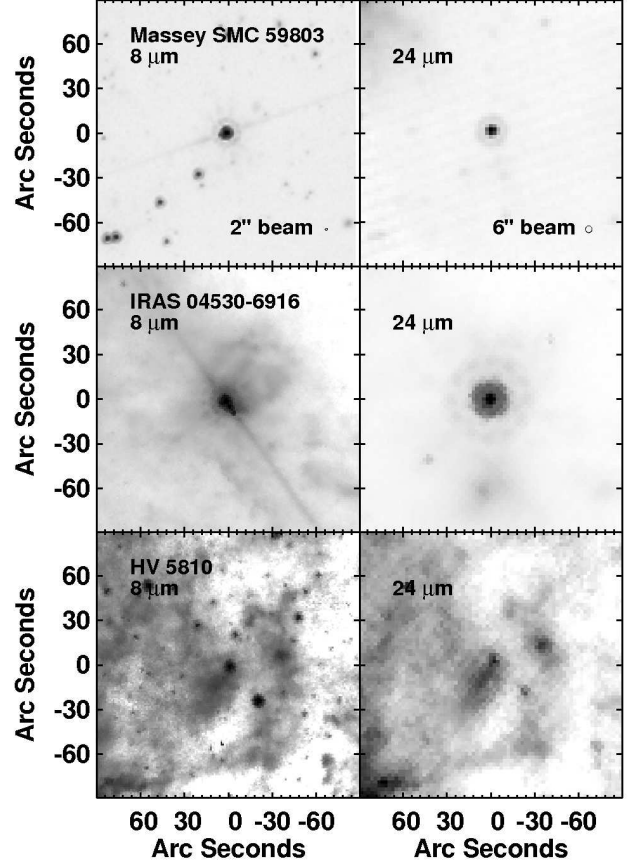


FIG. 23.— The 8 and 24 μm fields of the three PAH sources shown in Fig. 8 and 22. The images of Massey SMC 59803 and IRAS 04530 are plotted on a logarithmic scale, while HV 5810 is plotted on a linear scale. Massey SMC 59803 is an isolated supergiant, but the other two sources are associated with extended emission.

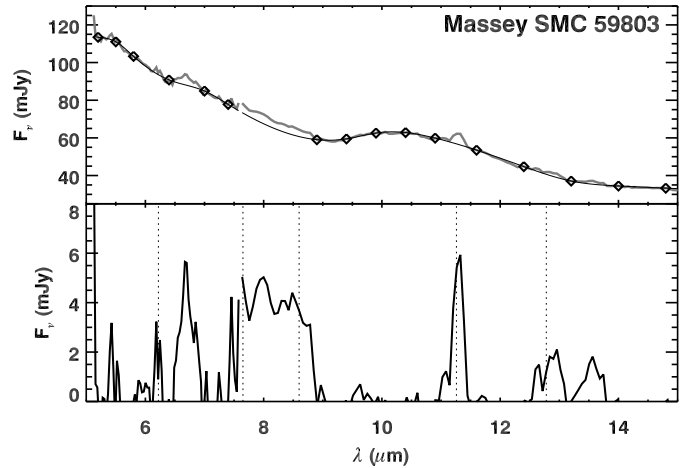


FIG. 24.— The spectrum of Massey SMC 59803 with a fitted spline (*top*), and the residual PAH spectrum (*bottom*). The dashed vertical lines in the bottom panel are at wavelengths of 6.23, 7.70, 8.60, 11.26, an 12.70 μm the centers of the PAH features in a typical class A PAH spectrum (in the classification system introduced by Peeters et al. 2002).

7.1. Massey SMC 59803

An examination of the 8 and 24 μm images of Massey SMC 59803 reveals no associated extended emission. The IRS data are also consistent with a point source at all wavelengths. To separate the contribution of PAHs from the spectrum, we fit a spline through the “continuum” from the star and amorphous silicate grains which produce the 10 μm feature, as illustrated in Figure 24 (top). Keller et al. (2008) applied this method to a sample of spectra from Herbig Ae/Be stars with both silicate and PAH emission and successfully disentangled the separate dust components in most cases.

Figure 24 (bottom) shows the resulting PAH spectrum. PAHs in the spectra of supergiants are unusual, but not unheard of. Sylvester et al. (1998) observed PAH emission at 8.6 and 11.3 μm in three supergiants in the η and χ Persei association. The residual PAH spectrum from Massey SMC 59803 shows emission features centered at 6.21, 6.70, 8.13, 11.29, 12.86, and 13.56 μm . The 6.7 μm feature probably does not arise from PAHs and is presently unidentified. The remaining features are from PAHs. The strongest features are the C–C complex centered at 8 μm and the out-of-plane C–H solo bending mode at 11.3 μm .

Peeters et al. (2002) defined three classes of PAH spectra based primarily on the position of the 8 μm PAH complex. Most spectra fell into class A (peak at 7.65 μm) or class B (7.85 μm), but two class C spectra showed a feature peaking at ~ 8.2 μm . The detailed position and shape of the 8 μm complex depends critically on how the spline fits the continuum on the blue side of the silicate feature, so we should not overinterpret this feature. Nonetheless, there does appear to be an excess between ~ 7.5 and 9 μm , and it is more consistent with class C than with the other classes. The 11.3 μm feature is also shifted from its nominal position in class A and B spectra of 11.26 μm (Sloan et al. 2007) to 11.29 μm .

Sloan et al. (2007) found that class C PAH spectra are associated with cooler radiation fields. Massey SMC 59803 has an estimated effective temperature of 4100 K (Levesque et al. 2006), and its PAH spectrum, while noisy, is consistent with this temperature.

7.2. HV 5810

As discussed in §4.2 and illustrated in Figure 6, the spectrum of HV 5810 shows emission from several C–H bending modes in PAHs. These include the in-plane bending modes at 8.55 and the out-of-plane bending modes at 11.27, 12.78, and 13.5 μm in SL (e.g. Allamandola et al. 1989; Hony et al. 2001). The emission at 12.78 μm probably contains a contribution from [Ne II] emission as well. The LL portion of the spectrum in Figure 24 reveals an emission complex in LL with peaks at 16.5 and 17.35 μm , which also arises from PAHs (Moutou et al. 2000; Werner et al. 2004b).

Examination of the spectral images reveals that the emission features at 11.3 and 12.8 μm extend the length of the SL slit. The emission at 8.6 μm is also extended. In the LL images, the 16–18 μm PAH complex is extended over about $\sim 20''$, while several forbidden emission lines are extended over much larger areas: [Ne III] at 15.6 μm , [S III] at 18.7 and 33.5 μm , and [Si II] at 34.8 μm . The forbidden lines are commonly seen in many images of

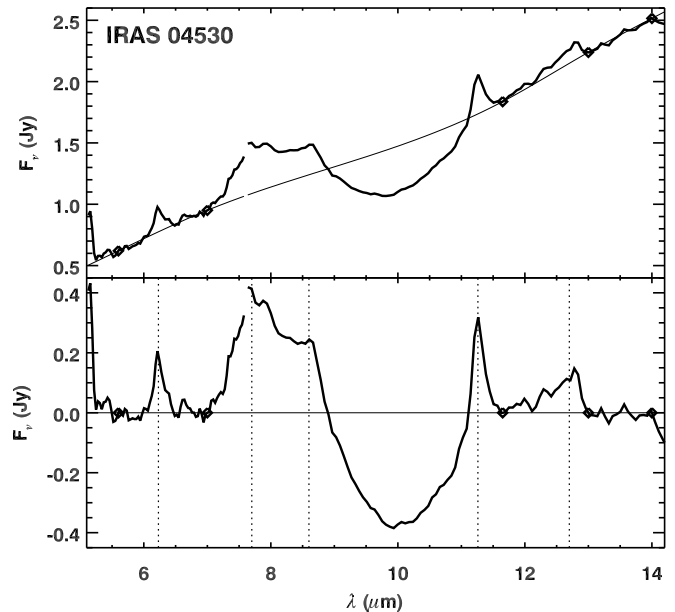


FIG. 25.— The SL spectrum of IRAS 04530, scaled to match the *IRAS* photometry. In the top panel, the spline points are marked with diamonds, and the fitted spline with a smooth thin curve. The spline-subtracted spectrum appears in the bottom panel, showing both silicate absorption and PAH emission. The vertical dotted lines are at wavelengths of 6.23, 7.70, 8.60, 11.26, and 12.70 μm .

other targets, but they usually subtract out when the background is removed. At longer wavelengths, the spatial structure of HV 5810 grows more complex and extended as well.

Figure 23 shows that HV 5810 is embedded in a complex region of extended emission. We conclude that we have observed a naked star, HV 5810, superimposed on a complicated background.

7.3. IRAS 04530–6916

The observations of IRAS 04530 were partially mispointed in both SL and LL, requiring some special attention to complete the processing. The source was mostly out of the slit in one of the SL nod positions, and in LL, we only observed a portion of the source, which is extended. To stitch the spectral segments together, we normalized them to the 12 and 25 μm fluxes from the *IRAS* Faint Source Catalog (2.01 and 4.97 Jy, respectively). Because of the spectral tilts in mispointed spectra, this leaves a discontinuity at the SL/LL interface. The overall continuum properties of the resulting spectrum should be considered provisional. Despite the limitations of the spectrum, the presence of various spectral features and their wavelengths are reliable.

The spectrum shows a combination of silicate absorption and emission from PAHs. Although the IRS does not cover the 35–45 μm wavelength range that the Hanscom system used to distinguish the reddest sources, the *IRAS* data show that the spectrum continues to rise between 25 and 60 μm , making this spectrum class 5.U/SA (this class was introduced by Engelke et al. 2004).

The combination of both PAH emission and silicate absorption complicates the analysis of the PAH strengths, but it does not have a significant effect on their positions. To examine the PAH features more closely, we fit a spline through the most likely continuum, as Figure

TABLE 9
FRACTION OF NAKED OXYGEN-RICH
STARS

Sample	Period (days)		
	≤ 250	250–700	> 700
Galaxy	2 of 106	5 of 269	0 of 11
LMC	2 of 3	2 of 9	0 of 8
SMC	1 of 1	6 of 7	0 of 1

25 illustrates. The resulting PAH spectrum has features peaking at 6.22, 7.65, 8.62, 11.27, and 12.78 μm . With the exception of the last feature, which may be affected by [Ne II] emission, the wavelengths for these features correspond to a class A PAH spectrum in the scheme of Peeters et al. (2002). This class of PAH spectrum is commonly seen in star formation regions.

IRAS 04530 has usually been treated as an evolved star. Wood et al. (1992) measured its bolometric magnitude to be -7.62 and concluded that it was probably a supergiant due to its high luminosity, low pulsation amplitude, and lack of maser activity. van Loon et al. (2001) seconded this opinion, and on the basis of these works it was included in this study. van Loon et al. (2005a) recently suggested that it may instead be a YSO. Their optical spectrum shows strong hydrogen emission lines as well as the [S III] doublet and [Ca II] triplet. Hodge et al. (2004) and Engelke et al. (2004) found that the U/SA classification in the *ISO* PHOT-S and CAM-CVF databases occurred almost exclusively in YSOs, star forming regions, and starburst galaxies (the single exception being C* 1662).

The SAGE images at 8 μm and 24 μm in Figure 23 reveal that IRAS 04530 lies at the edge of an extensive region of 8 μm emission probably associated with the DEM L15 H II region. The IRAC and MIPS photometry of IRAS 04530 (from the 2006 December release of the SAGE point source catalog Meixner et al. 2006) and the 2MASS photometry help clarify its evolutionary status. IRAS 04530 does not lie near the AGB population in the color-color and color-magnitude diagrams published from Galactic and Magellanic Spitzer programs (Whitney et al. 2003a,b; Blum et al. 2006; Bolatto et al. 2007).

In summary, evidence from the new *Spitzer* observations, both spectroscopic and photometric, support the suggestion of van Loon et al. (2005a) that IRAS 04530 is a YSO, not an evolved star.

8. DEPENDENCIES ON METALLICITY

The previous sections concentrated on the analysis applied to the different classes of spectra and the results for individual sources. This section concentrates on the samples as a whole, comparing the SMC and LMC samples to the Galactic samples published elsewhere. The dominant difference between these samples is metallicity.

8.1. Fraction of naked stars

Our sources were selected using criteria similar to those for the Galactic samples of AGB stars examined by Sloan & Price (1995) and supergiants studied by Sloan & Price (1998). The Galactic samples were chosen

TABLE 10
DUST EMISSION CONTRASTS

Sample	Period (days)		
	≤ 250	250–700	> 700
Galaxy	0.38 ± 0.27	0.61 ± 0.41	1.24 ± 0.61
LMC	0.06 ± 0.11	0.44 ± 0.30	2.29 ± 0.92
SMC	$0.06 \pm \dots$	0.07 ± 0.07	$0.80 \pm \dots$

by searching for optically identified variables of classes associated with either the AGB or supergiants in the LRS Atlas (IRAS Science Team 1986). Sloan & Price (1995) found that 43% of irregular (Lb) variables, 19% of semi-regular (SRb) variables, and only 1% of Mira variables (including SRA variables) were naked, while Sloan & Price (1998) found that 13 of 65, or 20%, of the supergiants were naked.

The MC_DUST sample includes five supergiants, all of which are associated with circumstellar dust, but the situation is different for the AGB. In the LMC, three of the 19 oxygen-rich sources, or 16%, are naked (we are excluding the naked star J052832, about which little is known), while in the SMC, seven of nine oxygen-rich AGB sources, or 78%, are naked.

We know the pulsation periods of enough of the various samples to compare how the fraction of naked stars varies with period in the Galaxy, LMC, and SMC. Because the number of naked stars is small, we divide the periods into only three bins separated at 250 d, the approximate boundary between most of the short-period semi-regulars and Miras, and 700 d, the approximate period limit for Miras in the Galactic sample. For the Galactic sample, we use the catalog published by Sloan & Price (1998). Of the 611 oxygen-rich AGB stars and supergiants in that catalog, 386 have periods, and only seven of those are naked. Two of the naked stars have periods less than 250 days, and the other five fall in the 250–700-day bin, as Table 9 shows. If we limited the sample to just Miras, the results are similar, with only two naked Miras out of 229.

Table 9 reveals that in the two lower-period bins, the percentage of naked stars increases as the metallicity of the sample decreases. None of the stars with periods greater than 700 days are naked. In the SMC, the only variable with a period less than 700 days and a dust excess is BFM 1, but even its dust shell is thin, and the dust spectrum is unusual.

8.2. Dust Emission Contrast

As part of the classification process in §5.1, we also measured the dust emission contrast for each oxygen-rich source, as defined for the naked stars in our sample. Figure 26 plots the dust emission contrast as a function of period in the Magellanic and Galactic samples for the naked and oxygen-rich sources. For periods between 250 and 700 days, the range dominated by Mira variables, the Galactic sample shows a general trend of increasing dust emission contrast with increasing period, but with a substantial spread. For periods less than 700 days, the Magellanic sources show significantly less dust emission than their Galactic counterparts. This result is consistent with the low SiO molecular band strength detected in naked oxygen-rich stars in the Magellanic Clouds, since SiO is

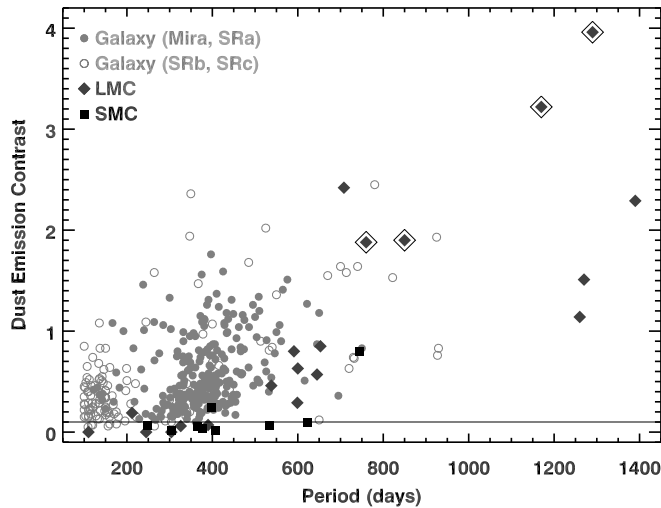


FIG. 26.— Dust emission contrast among oxygen-rich sources as a function of period, for all variables with known periods in the Galactic LRS sample (Sloan & Price 1995, 1998) and the MC_DUST sample. Dust emission contrast is defined in §3.4. In the Galactic sample, Miras and the closely related SRa variables are plotted as filled circles, while the SRb and SRc variables are plotted as open circles. LMC sources appear as dark gray diamonds, and SMC sources as black squares. The four symbols outlined in black mark suspected massive stars. The two points with periods ~ 800 days are supergiants. The two in the upper right are massive AGB sources (§3.3). The horizontal line at $\text{DEC} = 0.10$ separates naked and dusty sources in the Magellanic samples.

the basic building block of silicate dust.

Magellanic sources with periods greater than 700 days typically show large contributions from dust in their spectra. In particular, five sources lie on or appear to continue the trend of DEC vs. period established by the Galactic sample. Two of these sources, HV 888 and HV 996, are definite supergiants (at $\text{DEC} \sim 1.9$ and $P \sim 800$ d). Two more, IRAS 04509 and IRAS 04512, are probably very luminous AGB sources as discussed in §3.3. We believe these four sources are more massive than typical AGB sources and therefore younger. Since they formed more recently, they are probably more metal rich than typical Magellanic sources, and they would be expected to mimic the more metal-rich Galactic sample.

Figure 26 includes three more LMC sources with very long pulsation periods to the lower right. From top to bottom, these are IRAS 05402 ($\text{DEC} \sim 2.3$), IRAS 04545 ($\text{DEC} \sim 1.5$), and IRAS 05329 ($\text{DEC} \sim 1.1$). All three of these sources show silicate absorption at $10 \mu\text{m}$, so our DEC measurement, which is a simple sum, underestimates the total silicate contribution. Correcting for this simplification would undoubtedly push these points upward in Figure 26. However, all three spectra show clear evidence for crystalline silicate emission at longer wavelengths, which as described in §5.2, resemble the spectra from dusty Galactic objects with disks. This semblance is far from direct evidence of a disk, but it might indicate that presence of a reservoir of dust in addition to the dust forming in the outflows from these stars at the current time.

Table 10 presents the mean dust emission contrasts for the same period ranges used for Table 9. For the stars with periods ≤ 700 days, the amount of dust drops from the Galaxy to the LMC and drops further in the SMC. For these stars, the amount of dust clearly depends

TABLE 11
COMPARATIVE SiO BAND
STRENGTHS

Sample	W (μm)
SWS M giants	0.35 ± 0.11
IRS M giants	0.28 ± 0.06
LMC	0.26 ± 0.11
SMC	0.16 ± 0.08

on metallicity. As described above, the samples with periods > 700 days probably include young massive stars which blur the dependence on metallicity seen at shorter periods.

8.3. SiO band strengths

Matsuura et al. (2005) obtained $3\text{--}4 \mu\text{m}$ spectra of six oxygen-rich evolved stars in the LMC, and they detected possible weak SiO absorption in only one source, IRAS 05218, which had been thought to be a carbon star (Trams et al. 1999). They explained the absence of this band by noting that silicon is not produced in AGB stars, so its abundance in the photosphere reflects the initial abundance of the star, which will be low in a metal-poor system like the LMC. But at least four of their six targets have circumstellar dust shells, which make it possible that the dust partially masks the SiO bands.

In the MC_DUST sample, the SiO fundamental band is clearly present in the spectra of several of the less obscured sources. Table 11 compares the mean equivalent widths of the total LMC and SMC samples to two Galactic samples, one based on SWS observations and a second based on IRS data. For the SMC and LMC samples, we use only those equivalent widths in Table 6 with a S/N of ~ 1 or better. For sources with only an upper limit, we use it in place of the measured width. For HV 2575 (first observation), we take the upper limit to be $0.26 \mu\text{m}$. The follow-up spectra are treated as separate data. MACHO 79.5505.26 is not included since it may be carbon rich.

Using ISO/SWS data, Heras et al. (2002) determined that the strength of the SiO fundamental band increases from an equivalent width of $\sim 0.05 \mu\text{m}$ in K0 giants to $\sim 0.18 \mu\text{m}$ at K5. No M giant had an equivalent width less than ~ 0.15 , while the maximum value increased past $0.25 \mu\text{m}$ at M5. They measured the SiO equivalent width between 7.6 and $9.0 \mu\text{m}$, but the bandhead is at $7.4 \mu\text{m}$, and the band continues to $11.0 \mu\text{m}$ in some cases. We have remeasured the SiO fundamental band in their sample of 23 M giants using a similar method to that applied to the IRS data, except that we integrate the equivalent width directly instead of fitting a template absorption band. We shifted the long-wavelength range for fitting the Planck function from $11.5\text{--}13.0 \mu\text{m}$ to $10.8\text{--}11.4 \mu\text{m}$ to avoid hysteresis effects in the SWS data, which tend to drive the flux up slightly toward $12 \mu\text{m}$. For similar reasons, we shifted the long-wavelength boundary for integrating the equivalent width from 11.5 to $11.1 \mu\text{m}$. These shifts slightly reduce the equivalent widths, but the Galactic sample still has stronger SiO absorption than the Magellanic samples. The mean SiO equivalent width shows no strong dependency on optical spectral type.

The second comparison sample of M giants comes from

the ongoing IRS GTO Cycle 4 program used to generate the SiO template described in §4.1. At the time of this writing, spectra of 13 of the 20 planned M giants have been obtained and reduced. We extracted the SiO equivalent width using wavelengths identical to those used for the Magellanic samples, but as with the SWS data, we simply integrated the feature, instead of fitting a template. As with the SWS sample, the equivalent width does not depend strongly on spectral type. The difference between the two Galactic M giant samples may result from different selection criteria, but it is within the standard deviations.

Table 11 shows a general trend toward decreasing SiO band strength with decreasing metallicity, although there is some overlap in the samples. The LMC sample overlaps the IRS M giants. The wide spread in the LMC sample may indicate a range of metallicities, but the sample is not large. The SMC clearly shows weaker SiO bands than the Galactic giants. These results confirm the metallicity-dependent trend first recognized by Matsuura et al. (2005) in the $3\ \mu\text{m}$ spectral region.

8.4. Oxygen-rich dust composition

Egan & Sloan (2001) demonstrated with radiative transfer models that the amorphous alumina grains produce the broad, low-contrast features peaking $\sim 11\text{--}12\ \mu\text{m}$, which correspond to lower SE indices (SE1–3), while amorphous silicate grains produce the classic $10\ \mu\text{m}$ silicate feature (and associated $18\ \mu\text{m}$ feature) which corresponds to higher SE indices (SE6–8). The middle portion of the sequence (SE4–6) generally shows structured emission features, with a peak at $10\ \mu\text{m}$ and a shoulder at $11\ \mu\text{m}$. This structure could arise from multiple causes, including mixtures of amorphous alumina and silicates, self-absorbed silicates, or possibly, crystalline silicate grains. Given that alumina and silicates both contribute to the spectra, it might be more appropriate to refer to the sequence as the oxygen-rich dust sequence.

Figure 27 compares the distribution of silicate emission sources in the Magellanic Clouds to the Galactic samples examined by Sloan & Price (1995, 1998). The Magellanic sample differs markedly from the Galactic AGB sample by having only two sources from SE1 to SE4. In fact, it looks more like the Galactic supergiant sample than anything else, which is somewhat surprising given that the sample displayed in Figure 27 includes only three supergiants. We had intentionally observed ten stars classified as S or MS, which we had expected to resemble the Galactic S and MS stars, but most of these proved to be naked instead. Of the five S and MS stars in the LMC, three (WBP 104, HV 2575, and HV 12620) are naked, while HV 12070 is an SE6 and WBP 77 accounts for the lone SE1 source. Of the five in the SMC, only BFM 1 shows any sign of dust, but as discussed in §5.6., it is very unusual dust.

The lack of emission from amorphous alumina dust in the Magellanic Clouds is consistent with how the abundance of Al depends on metallicity compared to other dust-producing elements like Mg and Si. The latter elements are both α -capture products, and while their abundance is lower in metal-poor stars, Al is even less abundant (see Wheeler et al. 1989, and references therein).

The apparent absence of a $13\ \mu\text{m}$ feature in our

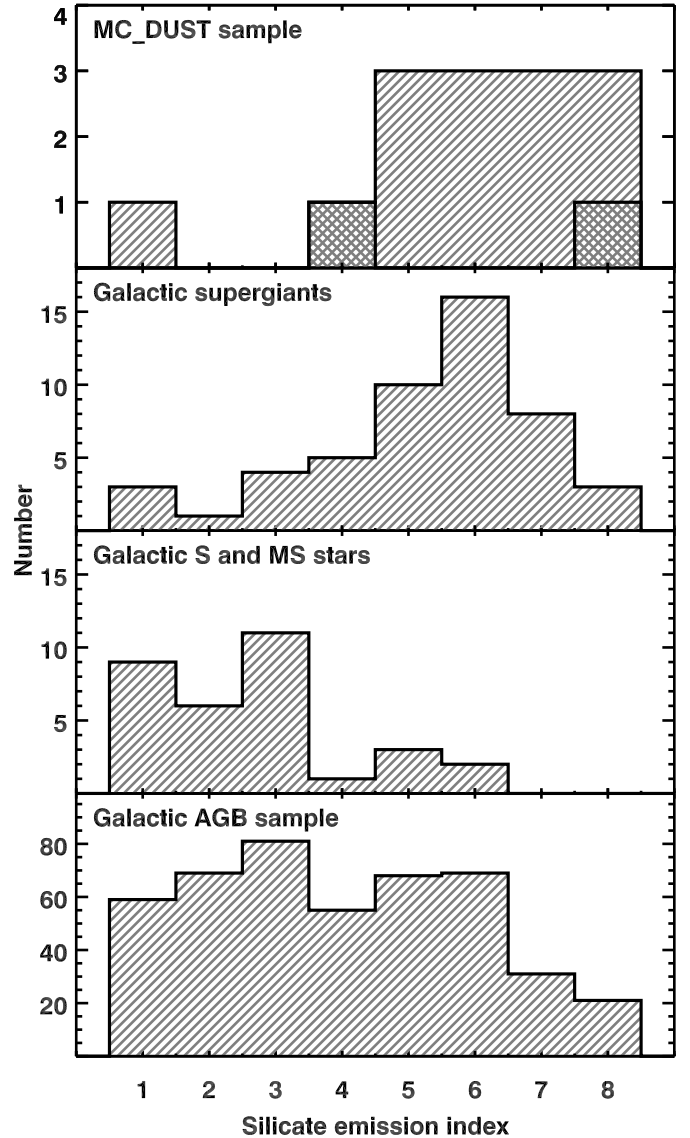


FIG. 27.— The distribution of the MC_DUST sample and Galactic comparison samples with silicate emission index. In the top panel, LMC sources are shaded with diagonal stripes, while the two SMC sources are cross-hatched (at SE4 and SE8). Alumina-rich dust produces the SE1–3 spectra and is largely absent from the Magellanic samples. The dust distribution in the Magellanic sample closely resembles the Galactic supergiants, even though only about three of the 14 Magellanic sources plotted in the upper panel are actually supergiants.

sample provides further evidence of the relative lack of Al in the Magellanic Clouds. The carrier of the $13\ \mu\text{m}$ feature has been the subject of some debate, with the focus on crystalline alumina (corundum, Al_2O_3 Glaccum 1994; Sloan et al. 1996) or spinel (MgAl_2O_4 Posch et al. 1999; Fabian et al. 2001a). Sloan et al. (2003) and DePew et al. (2006) have provided strong evidence against spinel as the carrier, but here, it is sufficient to note that in both proposed carriers, the Al–O bond is responsible for the $13\ \mu\text{m}$ feature. Consequently, the lack of Al in the Magellanic Clouds fully explains its absence.

The presence of the $14\ \mu\text{m}$ feature in our Magellanic sample provides some clues about its carrier. Pitman et al. (2006) recently noted that the $14\ \mu\text{m}$ feature in HV 2310 could be reproduced by AlN dust or pos-

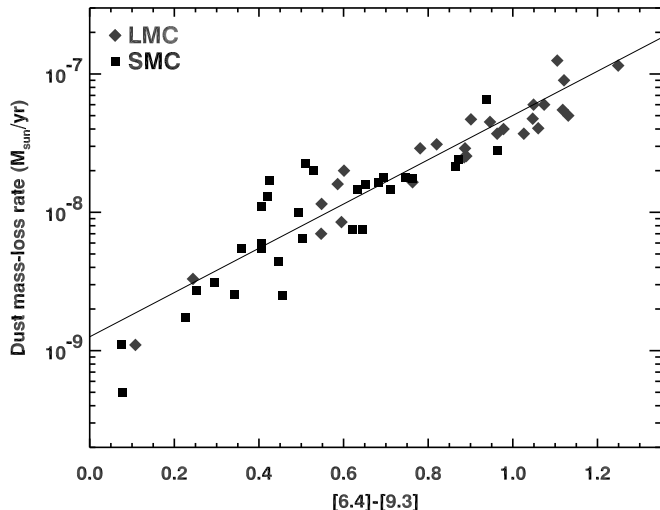


FIG. 28.— Dust mass-loss rate as a function of $[6.4]-[9.3]$ color, including data from the samples of Magellanic carbon stars presented by Sloan et al. (2006b); Zijlstra et al. (2006) and Lagadec et al. (2007) and analyzed with radiative transfer models by Groenewegen et al. (2007). We have converted the total mass-loss rates to dust mass-loss rates by dividing by their assumed gas-to-dust ratio of 200. The solid line is a linear fit to the data.

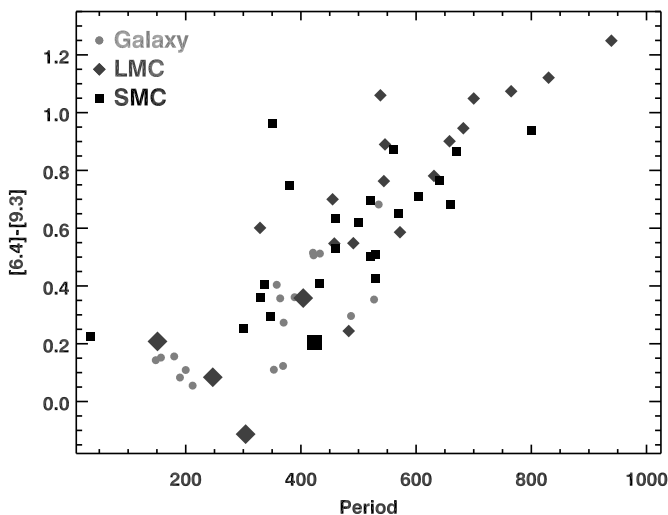


FIG. 29.— $[6.4]-[9.3]$ color as a function of period. The data include the samples from Fig. 22 (small diamonds and squares), the MC.DUST sample (large diamonds and squares), and the Galactic sample (small circles). The Galaxy, SMC, and LMC show no significant differences despite their different metallicities.

sibly by non-spherical corundum grains. While the non-spherical grain models discussed by DePew et al. (2006) do shift the emission peak from $13 \mu\text{m}$ to longer wavelengths, the features become quite broad compared to the observed $14 \mu\text{m}$ features. In addition, the low abundance of Al in the Magellanic Clouds make any Al-bearing dust species an unlikely carrier. The presence of the $14 \mu\text{m}$ feature appears to be limited to strong silicate emission sources, which suggests that its carrier is probably related to silicates in some way.

8.5. Carbon mass-loss rates

Grains composed primarily of carbon atoms, usually described as amorphous carbon, dominate the dust produced by carbon stars (e.g. Martin & Rogers 1987; Sloan & Egan 1995), but amorphous carbon has no eas-

ily discernable spectral features, making a direct measurement of its contribution difficult. The Manchester method substitutes the $[6.4]-[9.3]$ color, which will grow increasingly red as the contribution of amorphous carbon relative to the star increases. Groenewegen et al. (2007) applied radiative transfer models to all of the Magellanic carbon stars in the previously cited papers, and they found a good correlation between total mass-loss rate and $[6.4]-[9.3]$ color (see their Fig. 7). What the radiative transfer models actually probe, however, is the *dust* mass-loss rate. The total mass-loss rate is simply inferred from the gas-to-dust ratio, which Groenewegen et al. (2007) assumed to be 200 in both the LMC and SMC. We convert their mass-loss rates to dust mass-loss rates (by dividing by 200) and repeat their comparison to $[6.4]-[9.3]$ color in Figure 28. Both the LMC and SMC follow the same relation. Fitting a line to the data gives $\log(\text{mass-loss rate}) = -9.8 + 1.6([6.4]-[9.3])$. The scatter of the data about this line has a standard deviation of 16%.

This and previous studies have compared objects in the Galaxy, SMC, and LMC at similar $[6.4]-[9.3]$ color as though objects with similar amounts of amorphous carbon dust are truly alike. They might not be if the dust formation efficiency depended on metallicity. To examine this possibility, we examined the pulsation periods of the sources in the various samples, since those should be similar for physically similar stars. Figure 29 plots $[6.4]-[9.3]$ color as a function of pulsation period, and it reveals no significant differences in the distribution of colors at a given period between the samples. In other words, carbon stars with similar pulsation properties are embedded in similar quantities of dust, regardless of their initial metallicity.

9. DISCUSSION AND CONCLUSIONS

The similar dust production rates among the samples in Figure 29 have important consequences. The production of amorphous carbon is limited by the amount of excess carbon compared to oxygen, but carbon is produced in the triple- α process in AGB stars. The production of silicates and other oxygen-rich grains, on the other hand, is limited by the abundances of heavy elements such as Si and Al, and these are not produced in significant quantities on the AGB. The ready explanation for the results presented in Figure 29 is that the carbon produced and dredged up by AGB stars dominates the carbon with which they formed. It should follow, then, that even Population III stars, if they are in the mass range to become carbon stars, will produce approximately the same amount of carbon-rich dust as their Population I counterparts.

Blanco et al. (1978, 1980) discovered that in the SMC, more AGB stars became carbon rich than in the LMC (see also Cioni & Habing 2003). Renzini & Voli (1981) explained this phenomenon as a metallicity effect. Stars with solar abundances will become carbon stars if their initial mass $\gtrsim 1.7 M_{\odot}$, but at 1/5 solar metallicity, the mass limit has dropped to $1.2 M_{\odot}$, primarily because of the lack of oxygen in the atmosphere of the metal-poor star to balance the dredged up carbon. Assuming a Salpeter initial mass function (Salpeter 1955) and integrating from these carbon limits to $8 M_{\odot}$, we find that in the SMC, 70% more of the AGB should be carbon-rich

compared to a sample with solar metallicity. Since we see no diminishment of carbon-rich dust production at decreasing metallicity, we conclude that the more metal-poor an initial population of stars, the more carbon-rich dust it will contribute to the ISM, simply because it produces more carbon stars.

Many other properties of carbon stars do depend on metallicity. Our small sample reinforces results from previous studies of *Spitzer* spectroscopy in the Magellanic Clouds, which show that as the metallicity decreases, emission from SiC and MgS dust decrease, while absorption from acetylene gas increases. The increased acetylene absorption probably arises from higher C/O ratios in Magellanic carbon stars (van Loon et al. 1999; Matsuura et al. 2002, 2005), which in turn arise from a combination of increased dredge-up efficiency (Wood 1981) and less initial oxygen in the atmosphere (Vassiliadis & Wood 1993). The additional acetylene we observe may add even more to the amount of carbon injected into the ISM by metal-poor populations.

The behavior of the oxygen-rich dust stands in stark contrast to the carbon-rich dust. While the quantity of carbon-rich dust shows no discernable dependence on metallicity, oxygen-rich dust shows many clear trends. As metallicity decreases, (1) the fraction of naked stars increases, (2) SiO absorption decreases, (3) the silicate dust emission also decreases, and (4) alumina-rich dust emission disappears almost entirely. The lower metallicity of the Magellanic Clouds provides a ready explanation for all of these effects. Si is not produced on the AGB, so its abundance scales with overall metallicity. As a result, we observe less SiO gas, which is the fundamental building block of silicate dust, and less silicate dust as well. The abundance of Al scales even more strongly with metallicity (§5.4.), so the lack of alumina dust should not be a surprise. Not only do we see few spectra in the SE1–3 range, but we see little or no emission from the 13 μ m feature, which arises from an Al–O bond.

Standard condensation sequences propose the formation of alumina-rich grains before silicates (e.g. Tielens 1990; Stencel et al. 1990). The lack of alumina dust in our sample suggests the formation of alumina is not a prerequisite to the formation of silicates. In other words, silicates can form without pre-existing alumina grains to serve as seeds.

The oxygen-rich sample contains a wealth of interesting dust features. Five sources show crystalline silicate features at 10 μ m or longer wavelengths, and these are all consistent with Mg-rich pyroxene and olivine. There is no evidence for Fe in the silicates, much like the Galactic sample. Several sources have an unidentified 14 μ m emission feature, and one source, the only true S star in our sample, shows a previously unknown 13.5 μ m emission feature. These two features are newly discovered by the IRS, and their identification awaits further investigation.

The Magellanic Clouds present us with a scenario of steady or increasing carbon-rich dust production as systems grow more metal-poor, compared to declining rates of oxygen-rich dust production. This result measures

what goes into the ISM, but it contradicts observations of what is currently present in the ISM in metal-poor systems. Most lines of sight in the SMC have unusual extinction curves without the commonly observed 2175 Å bump seen in the Galaxy, in common with starburst galaxies and quasars (e.g. Gordon & Clayton 1998; Pitman et al. 2000, and references therein). The 2175 Å bump is commonly associated with graphitic carbonaceous material (as first proposed by Stecher & Donn 1965). Duley & Seahra (1998) showed that certain PAHs and PAH clusters can reproduce the 2175 Å bump and that these particles can result from interstellar processing of hydrogenated amorphous carbon. The recent study of unusual PAH-like spectra by Sloan et al. (2007) demonstrates that hydrocarbons can exist with a range of aromatic-to-aliphatic ratios. Many of the sources of unusual PAH-like emission are carbon-rich post-AGB objects. All of these observations support an evolutionary relationship from amorphous carbon produced by carbon stars on the AGB and to interstellar PAHs to the more graphitic material responsible for the 2175 Å bump. The results in this paper demonstrate that carbon-rich dust production does not decrease in more metal-poor samples, and yet, metal-poor systems like the SMC are missing the 2175 Å bump that should result.

Either the missing carbon-rich dust did not form, or it has been destroyed. Gordon & Clayton (1998) suggested that harsher radiation fields in metal-poor systems can destroy the carrier of the 2175 Å bump. Stellar modelling shows that decreasing the metallicity of a star results in less UV line blanketing and an emitted spectrum with more UV emission (Giveon et al. 2002), which readily explains the harsher interstellar radiation observed in metal-poor H II regions (Martín-Hernández et al. 2002). Galliano et al. (2008) recently reached the opposite conclusion. They used galactic evolution models to investigate the absence of PAH emission in blue compact dwarf galaxies and other metal-poor galaxies (Engelbracht et al. 2005; Wu et al. 2006), and concluded that these systems produce significantly less carbon-rich dust than the Galaxy. Our sample of Magellanic carbon stars provides no evidence for less carbon-rich dust formation in more primordial systems, which leads to the conclusion that the lack of carbon-bearing dust in these systems results not from reduced production, but from enhanced destruction.

The authors thank the anonymous referee for carefully reading the manuscript and helping us to improve it. These observations were made with the *Spitzer Space Telescope*, which is operated by JPL, California Institute of Technology under NASA contract 1407 and supported by NASA through JPL (contract number 1257184). This research has made use of the SIMBAD and VIZIER databases, operated at the Centre de Données astronomiques de Strasbourg, and the Infrared Science Archive at the Infrared Processing and Analysis Center, which is operated by JPL.

REFERENCES

- Alcock, C., et al. 1996, *ApJ*, 461, 84
 Allamandola, L. J., Tielens, A. G. G. M., & Barker, J. R. 1989, *ApJS*, 71, 733
 Alves, D. R. 2004, *New Astron. Rev.* 2004, 48, 659
 Bergeat, J., & Chevallier, L. 2005, *A&A*, 429, 235

- Bernard-Salas, J., Peeters, E., Sloan, G. C., Cami, J., Guiles, S., & Houck, J. R. 2007, *ApJ*, 652, L29
- Blanco, B. M., Blanco, V. M., & McCarthy, M. F. 1978, *Nature*, 271, 638
- Blanco, V. M., Blanco, B. M., & McCarthy, M. F. 1980, *ApJ*, 242, 938
- Blanco, V. M., Frogel, J. A., & McCarthy, M. F. 1981, *PASP*, 93, 532
- Blum, R. D., et al. 2006, *AJ*, 132, 2034
- Bolatto, A. D., et al. 2007, *ApJ*, 655, 212
- Buchanan, C. L., Kastner, J. H., Forrest, W. J., Hrivnak, B. J., Sahai, R., Egan, M., Frank, A., & Barnbaum, C. 2006, *AJ*, 132, 1890
- Cami, J. 2002, Ph.D. Thesis, Univ. of Amsterdam
- Cernuschi, F., Marsiano, F., & Codina, S. 1967, *Ann. d'Ap.*, 30, 1039
- Chihara, H., Koike, C., Tsuchiyama, A., Tachibana, S., & Sakamoto, D. 2002, *A&A*, 391, 267
- Cioni, M.-R. L. & Habing, H. J. 2003, *A&A*, 402, 133
- DePew, K., Speck, A., & Dijkstra, C. 2006, *ApJ*, 640, 971
- Dessy, J. L. 1959, *Bol. Inst. Mat. Astr. Fis. Cordoba*, Vol. 1, No. 2
- Duley, W. W. & Seahra, S. 1998, *ApJ*, 507, 874
- Dwek, E. & Scalo, J. M. 1980, *ApJ*, 239, 193
- Egan, M. P., van Dyk, S. D., & Price, S. D. 2001, *AJ*, 122, 1844
- Egan, M. P., et al. 2003, "The Midcourse Space Experiment Point Source Catalog, Version 2.3, Explanatory Guide," Air Force Research Laboratory Technical Report AFRL-VS-TR-2003-1589
- Egan, M. P. & Sloan, G. C. 2001, *ApJ*, 558, 165
- Emery, J. P., Cruikshank, D. P., van Cleve, J. 2006, *Icarus*, 182, 496
- Engelbracht, C. W., Gordon, K. D., Rieke, G. H., Werner, M. W., Dale, D. A., & Latter, W. B. 2005, *ApJ*, 628, L29
- Engelke, C. W., Kraemer, K. E., & Price, S. D. 2004, *ApJS*, 150, 343
- Fabian, D., Posch, Th., Mutschke, H., Kerschbaum, F., & Dorschner, J. 2001a, *A&A*, 373, 1125
- Fabian, D., Henning, T., Jäger, C., Mutschke, H., Dorschner, J., & Wehrhan, O. 2001, *A&A*, 378, 228
- Galliano, F., Madden, S. C., Tielens, A. G. G. M., Peeters, E., & Jones, A. P. 2008, *ApJ*, 679, 310
- Gehrz, R. 1989, in *Interstellar Dust*, *Proc. IAU Symp.* 135, ed. L. J. Allamandola & A. G. G. M. Tielens (Dordrecht: Kluwer Academic Publishers), 445
- Gillet, F. C., Low, F. J., & Stein, W. A. 1968, *ApJ*, 154, 677
- Givoe, U., Sternberg, A., Lutz, D., Feuchtgruber, H., & Pauldrach, A. W. A. 2002, *ApJ*, 566, 880
- Glaccum, W. 1994, in *Proc. of the Airborne Astronomy Symp. on the Galactic Ecosystem: From Gas to Stars to Dust*, ed. M. R. Haas, J. A. Davidson, & E. F. Erickson (San Francisco: ASP), 395
- Gordon, K. & Clayton, G. C. 1998, *ApJ*, 500, 816
- Groenewegen, M. A. T., et al. 2007, *MNRAS*, 376, 313
- Heras, A. M., Shipman, R. F., Price, S. D., de Graauw, Th., Walker, H. J., Jourdain de Muizon, M., Kessler, M. F., Prusti, T., Decin, L., Vandenbussche, B., Waters, L. B. F. M. 2002, *A&A*, 394, 539
- Hodge, T. M., Kraemer, K. E., Price, S. D., & Walker, H. J. 2004, *ApJS*, 151, 299
- Hony, S., Van Kerckhoven, C., Peeters, E., Tielens, A. G. G. M., Hudgins, D. M., & Allamandola, L. J. 2001, *A&A*, 370, 1030
- Houck, J. R., et al. 2004, *ApJS*, 154, 18
- Huber, K. P. & Herzberg, G. 1979, *Molecular Spectra and Molecular Structure*, Vol. IV. Constants of Diatomic Molecules (New York: Van Nostrand Reinhold Co.)
- IRAS Science Team 1986, *A&AS*, 65, 607
- Jäger, C., Molster, F. J., Dorschner, J., Henning, Th., Mutschke, H., Waters, L. B. F. M. 1998, *A&A*, 339, 904
- Kastner, J. H., Buchanan, C. L., Sargent, B., & Forrest, W. J. 2006, *ApJ*, 638, L29
- Keremidjiev, M. S. & Sloan, G. C., 2006, *IRS Technical Report 06001*
- Keller, L. D., Sloan, G. C., Forrest, W. J., Ayala, S., D'Alessio, P., Shah, S., Calvet, N., Hartmann, L., Najita, J., Sargent, B., Li, A., Watson, D. M., & Chen, C. H. 2008, *ApJ*, submitted
- Keller, S. C. & Wood, P. R. 2006, *ApJ*, 642, 834
- Koike, C., Chihara, H., Tsuchiyama, A., Suto, H., Sogawa, H., & Okuda, H. 2003, *A&A*, 399, 110
- Kraemer, K. E., Sloan, G. C., Price, S. D., & Walker, H. J. 2002, *ApJS*, 140, 389
- Kraemer, K. E., Sloan, G. C., Wood, P. R., Price, S. D., & Egan, M. P. 2005, *ApJ*, 631, L147
- Kraemer, K. E., Sloan, G. C., Bernard-Salas, J., Price, S. D., Egan, M. P., & Wood, P. R. 2006, *ApJ*, 652, L25
- Lagadec, E., Zijlstra, A. A., Sloan, G. C., Matsuura, M., Wood, P. R., van Loon, J. Th., Harris, G. J., Blommaert, J. A. D. L., Hony, S., Groenewegen, M. A. T., Feast, M. S., Whitelock, P. A., Menzies, J. W., & Cioni, M.-R. 2007, *MNRAS*, 376, 1270
- Lambert, D. L. & Clegg, R. E. S. 1980, *MNRAS*, 191, 367
- Leisenring, J. M., Markwick-Kemper, F., & Sloan, G. C. 2008, *ApJ*, in press
- Levesque, E. M., Massey, P., Olsen, K. A. G., Plez, B., Meynet, G., & Maeder, A. 2006, *ApJ*, 645, 1102
- Little-Marenin, I. R., & Price, S. D. 1986, in *Summer School on Interstellar Processes: Abstracts of Contributed Papers*, ed. D. J. Hollenbach & H. A. Thronson, NASA Tech. Memorandum 88342 (NASA Ames Research Center: Moffett Field, CA), 137
- Lutz, D., Sturm, E., Tacconi, L. J., Valiante, E., Schweitzer, M., Netzer, H., Maiolino, R., Andreani, P., Shemmer, O., & Veilleux, S. 2007, *ApJ*, 661, L25
- Maeder, A. 1992, *A&A*, 264, 105
- Markwick-Kemper, et al. 2008, in preparation
- Marshall, J. R., van Loon, J. Th., Matsuura, M., Wood, P. R., Zijlstra, A. A., & Whitelock, P. A. 2004, *MNRAS*, 355, 1348
- Martin, P. G. & Rogers, C. 1987, *ApJ*, 322, 374
- Martín-Hernández, N. L., Vermeij, R., Tielens, A. G. G. M., van der Hucht, J. M., & Peeters, E. 2002, *A&A*, 389, 286
- Matsuura, M., Zijlstra, A. A., van Loon, J. Th., Yamamura, I., Markwick, A. J., Woods, P. M., & Waters, L. B. F. M. 2002, *ApJ*, 580, L133
- Matsuura, M., Zijlstra, A. A., van Loon, J. Th., Yamamura, I., Markwick, A. J., Whitelock, P. A., Woods, P. M., Marshall, J. R., Feast, M. W., & Waters, L. B. F. M. 2005, *A&A*, 434, 691
- Matsuura, M., et al. 2006, *MNRAS*, 371, 415
- McGregor, P. J., Hart, J., Hoadley, D., & Bloxham, G. 1994, in *Infrared Astronomy with Arrays*, ed. I. McLean (Dordrecht: Kluwer), 299
- Meikle, W. P. S., Mattila, S., Pastorello, A., Gerardy, C. L., Kotak, R., Sollerman, J., Van Dyk, S. D., Farrah, D., Filippenko, A. V., Höflich, P., Lundqvist, P., Pozzo, M., & Wheeler, J. C. 2007, *ApJ*, 665, 608
- Meixner, M., et al. 2006, *AJ*, 132, 2268
- Min, M., Hovenier, J. W., & de Koter, A. 2003, *A&A*, 404, 35
- Molster, F. J., Waters, L. B. F. M., Tielens, A. G. G. M. 2002, *A&A*, 382, 222
- Moutou, C., Verstraete, L., Léger, A., Sellgren, K., & Schmidt, W. 2000, *A&A*, 354, L17
- Ossenkopf, V., Henning, T., & Mathis, J. S. 1992, *A&A*, 261, 567
- Peeters, E., Hony, S., Van Kerckhoven, C., Tielens, A. G. G. M., Allamandola, L. J., Hudgins, D. M., & Bauschlicher, C. W. 2002, *A&A*, 390, 1089
- Phillips, J. G. & Davis, S. P. 1979, *ApJ*, 229, 867
- Pitman, K. M., Speck, A. K., & Hofmeister, A. M. 2006, *MNRAS*, 371, 1744
- Pitman, K. M., Clayton, G. C., & Gordon, K. D. 2000, *PASP*, 112, 537
- Posch, T., Kerschbaum, F., Mutschke, H., Fabian, D., Dorschner, J., & Hron, J. 1999, *A&A*, 352, 609
- Renzini, A. & Voli, M. 1981, *A&A*, 94, 175
- Salpeter, E. E. 1955, *ApJ*, 121, 161
- Skrutskie, M. F., et al. 2006, *AJ*, 131, 1163
- Sloan, G. C., Devost, D., Bernard-Salas, J., Wood, P. R., & Houck, J. R. 2006, *ApJ*, 638, 472
- Sloan, G. C. & Egan, M. P. 1995, *ApJ*, 444, 452
- Sloan, G. C., Jura, M., Duley, W. W., Kraemer, K. E., Bernard-Salas, J., Forrest, W. J., Sargent, B., Li, A., Barry, D. J., Bohac, C. J., Watson, D. M., & Houck, J. R. 2007, *ApJ*, 664, 1144
- Sloan, G. C., Kraemer, K. E., Matsuura, M., Wood, P. R., Price, S. D., & Egan, M. P. 2006, *ApJ*, 645, 1118
- Sloan, G. C., Kraemer, K. E., Price, S. D., & Shipman, R. F. 2003, *ApJS*, 147, 379
- Sloan, G. C., LeVan, P. D., & Little-Marenin, I. R. 1996, *ApJ*, 463, 310
- Sloan, G. C. & Price, S. D. 1995, *ApJ*, 451, 758
- Sloan, G. C. & Price, S. D. 1998, *ApJS*, 119, 141

- Sloan, G. C., Zijlstra, A. A., Kraemer, K. E., Markwick-Kemper, F., & Leisenring, J. M. 2008, in *The Biggest, Baddest, Coolest Stars*, ed. R. E. Stencel & B. J. Smith
- Sloan, G. C., et al. 2008, MNRAS, in preparation
- Sloan, G. C., et al. 2008, AJ, in preparation
- Sloan, G. C., et al. 2008, ApJ, in preparation
- Smith, V. V., Plez, B., Lambert, D. L., Lubowich, D. A. 1995, ApJ, 441, 735
- Speck, A. K., Cami, J., Markwick-Kemper, C., Leisenring, J., Szczerba, R., Dijkstra, C., Van Dyk, S., & Meixner, M. 2006, ApJ, 650, 892
- Spinrad, H. & Wing, R. F. 1969, ARA&A, 7, 249
- Stecher, T. P. & Donn, B. 1965, ApJ, 142, 1681
- Stencel, R. E., Nuth, J. A., Little-Marenin, I. R., & Little, S. J. 1990, ApJ, 350, L45.
- Sugerman, B. E. K., et al. 2006, Science, 313, 196
- Suto, H., Sogawa, H., Tachibana, S., Koike, C., Karoji, H., Tsuchiyama, A., Chihara, H., Mizutani, K., Akedo, J., Ogiso, K., Fukui, T., & Ohara, S. 2006, MNRAS, 370, 1599
- Sylvester, R. J., Skinner, C. J., & Barlow, M. J. 1997, MNRAS, 301, 1083
- Szymański, M. K. 2005, Acta Astron., 55, 43
- Teplitz, H. I., Desai, V., Armus, L., Chary, R., Marshall, J. A., Colbert, J. W., Frayer, D. T., Pope, A., Blain, A., Spoon, H. W. W., Charmandaris, V., & Scott, D. 2007, ApJ, 659, 941
- Tielens, A. G. G. M. 1990, in *From Miras to Planetary Nebulae: Which Path for Stellar Evolution?*, ed. M. O. Mennessier & A. Omont (Gif-sur-Evette: Editions Frontières), 186
- Trams, N. R., van Loon, J. Th., Waters, L. B. F. M., Zijlstra, A. A., Loup, C., Whitelock, P. A., Groenewegen, M. A. T., Blommaert, J. A. D. L., Siebenmorgen, R., Heske, A., & Feast, M. W. 1999, A&A, 346, 843
- Udalski, A., Kubiak, M., & Szymáński, M. 1997, Acta Astron., 47, 319
- Valenti, J. A., Piskunov, N., Johns-Krull, C. M. 1998, ApJ, 498, 851
- van Loon, J. Th., Groenewegen, M. A. T., de Koter, A., Trams, N. R., Waters, L. B. F. M., Zijlstra, A. A., Whitelock, P. A., & Loup, C. 1999, A&A, 559, 572
- van Loon, J. Th., Zijlstra, A. A., Bujarrabal, V., & Nyman, L.-Å. 2001, A&A, 368, 950
- van Loon, J. Th., Cioni, M.-R. L., Zijlstra, A. A., & Loup, C. 2005, A&A, 438, 273
- van Loon, J. Th., Oliveira, J. M., Wood, P. R., Zijlstra, A. A., Sloan, G. C., Matsuura, M., Whitelock, P. A., Groenewegen, M. A. T., Blommaert, J. A. D. L., Cioni, M.-R. L., Hony, S., Loup, C., & Waters, L. B. F. M. 2005, MNRAS, 364, L71
- van Loon, J. Th., Marshall, J. R., Cohen, M., Matsuura, M., Wood, P. R., Yamamura, I., & Zijlstra, A. A. 2006, A&A, 447, 971
- van Loon, J. Th., Cohen, M., Oliveira, J. M., Matsuura, M., McDonald, I., Sloan, G. C., Wood, P. R., & Zijlstra, A. A. 2008, MNRAS, submitted
- Vassiliadis, E. & Wood P. R. 1993, ApJ, 413, 641
- Werner, M. W., et al. 2004a, ApJS, 154, 1
- Werner, M. W., Uchida, K. I., Sellgren, K., Marengo, M., Gordon, K. D., Morris, P. W., Houck, J. R., & Stansberry, J. A. 2004b, ApJS, 154, 309
- Wheeler, J. C., Sneden, C., & Truran, J. W., Jr. 1989, ARA&A, 27, 279
- Whitelock, P. & Feast, M. 2000, Mem. Soc. Astron. Ital. 71, 601
- Whitelock, P. A., Feast, M. W., van Loon, J. Th., & Zijlstra, A. A. 2003, MNRAS, 342, 86
- Whitney, B. A., Wood, K., Bjorkman, J. E., & Wolff, M. J. 2003a, ApJ, 591, 1049
- Whitney, B. A., Wood, K., Bjorkman, J. E., & Cohen, M. 2003b, ApJ, 598, 1079
- Woitke, P. 2006, A&A, 452, 537
- Wood, P. R. 1981, in *Physical Processes in Red Giants*, ed. I. Iben & A. Renzini, (Dordrecht: Reidel), 135
- Wood, P. R., Bessell, M. S., & Fox, M. W. 1983, ApJ, 272, 99
- Wood, P. R., Bessell, M. S., & Paltoglou, G. 1985, ApJ, 290, 477
- Wood, P. R., Whiteoak, J. B., Hughes, S. M. G., Bessell, M. S., Gardner, F. F., & Hyland, A. R. 1992, ApJ, 397, 552
- Wu, Y., Charmandaris, V., Hao, L., Brandl, B. R., Bernard-Salas, J., Spoon, H. W. W., Houck, J. R. 2006, ApJ, 639, 157
- Wyckoff, S. & Clegg, R. E. S. 1979, MNRAS, 184, 127
- Zijlstra, A. A., et al. 2006, MNRAS, 370, 1961